



# Small-Object Detection in Remote Sensing Images and Video

by

**Stamatios Orfanos**

Submitted

in partial fulfilment of the requirements for the degree of

Master of Artificial Intelligence

at the

UNIVERSITY OF PIRAEUS

July 2024

**Author.....** **Stamatos Orfanos**  
II-MSc “Artificial Intelligence”  
, 2024

**Certified by.....** **Ilias Maglogiannis**  
Professor  
Thesis Supervisor

**Certified by.....** **Theodoros Giannakopoylos**  
Researcher  
Member of Examination Committee

**Certified by.....** **Michael Filippakis**  
Professor  
Member of Examination Committee

# **Small-Object Detection in Remote Sensing Images and Video**

**By**

**Stamatis Orfanos**

Submitted to the II-MSc “Artificial Intelligence” on XX XX, 2024, in  
partial fulfilment of the  
requirements for the MSc degree

## **Abstract**

Object detection in remote sensing images has been a challenging problem for the computer vision research community because the objects in such images have very few pixels. There have been improvements in the mean Average Precision (mAP) of the models using different architectures. Most of the detection models are becoming more complex and bigger, which can cause a problem usually when a detection model is intended for use in a satellite or an Unmanned Aerial Vehicle, since their computation resources are limited. The thesis introduces a novel approach that has achieved a comparable in computational complexity, to the lightest models in the field. The model was able to achieve an substantial improvement on the Unmanned Aerial Vehicle Small Object Detection (UAV-SOD) and the Visual Drone (visdrone) datasets in the order of x% and y% accordingly, while maintaining an almost identical performance on the last and most complex dataset the Microsoft Common Object in COntext (MS COCO) at z%.

The results demonstrate the effectiveness of the proposed method, providing useful intel in multi-task learning and achieving better than most computational efficiency with detection performance for the utilized datasets.

**Thesis Supervisor:** Ilias Maglogiannis  
**Title:** Professor

# Contents

<b>1</b>	<b>Introduction</b>	<b>1</b>
<b>2</b>	<b>Related Work</b>	<b>3</b>
2.1	Multi-stage Object Detection Models . . . . .	3
2.1.1	Region-based Convolution Neural Networks . . . . .	4
2.1.2	Feature Pyramid Networks . . . . .	9
2.1.3	Vision Transformers . . . . .	11
2.2	Single-stage Object Detection Models . . . . .	14
2.2.1	You Only Look Once . . . . .	14
2.2.2	Single Shot MultiBox Detector . . . . .	16
<b>3</b>	<b>Methodology</b>	<b>17</b>
3.1	Architecture . . . . .	17
3.1.1	Extended Feature Pyramid Network . . . . .	19
3.1.2	Masked-Attention Mask Transformer . . . . .	20
3.1.3	Extended Masked-Attention Mask Transformer . . . . .	22
<b>4</b>	<b>Experiments</b>	<b>27</b>
4.1	Datasets . . . . .	27
4.1.1	Microsoft Common Object in COntext (MS COCO) . . . . .	27
4.1.2	Unmanned Aerial Vehicle Small Object Detection . . . . .	29
4.1.3	VisDrone . . . . .	30
4.2	Data Pre-Processing . . . . .	32
4.3	Evaluation Metrics . . . . .	33
4.4	Training . . . . .	35
4.5	Results . . . . .	36
4.5.1	Microsoft Common Object in COntext (MS COCO) . . . . .	36
4.5.2	Unmanned Aerial Vehicle Small Object Detection . . . . .	37
4.5.3	VisDrone . . . . .	38
<b>5</b>	<b>Discussion</b>	<b>40</b>
5.0.1	Differences between models . . . . .	40
5.0.2	Performance difference between datasets . . . . .	40
<b>6</b>	<b>Conclusion</b>	<b>41</b>
<b>A</b>	<b>Appendix A</b>	<b>44</b>

# List of Figures

2.1	Region-based Convolution Neural Network Architecture [12] . . . . .	4
2.2	Fast Region-based Convolution Neural Network Architecture [11] . . . . .	5
2.3	Faster Region-based Convolution Neural Network Architecture [23] . . . . .	6
2.4	Region Proposal Network [23] . . . . .	7
2.5	Mask Region Convolution Neural Network Architecture [13] . . . . .	7
2.6	Mask Region Of [13] . . . . .	8
2.7	Feature Pyramid Network [16] . . . . .	10
2.8	Feature Pyramid Network Top-Down path [16] . . . . .	10
2.9	NLP Transformer Architecture [9] . . . . .	11
2.10	Vision Transformer Architecture [9] . . . . .	12
2.11	YOLO Architecture [21] . . . . .	15
2.12	Single Shot MultiBox Detector Architecture [17] . . . . .	16
3.1	Small Object Detection Mapping [8] . . . . .	18
3.2	Extended Feature Pyramid Network [8] . . . . .	19
3.3	Feature Texture Transfer [8] . . . . .	19
3.4	Masked-Attention Mask Transformer [5] . . . . .	20
3.5	Extended Masked-Attention Mask Transformer . . . . .	22
3.6	Extended Masked-Attention Mask Transformer - Transformer Module . . . . .	23
4.1	Class Distribution in COCO 2017 . . . . .	28
4.2	Class Distribution in UAV Small Object Detection . . . . .	29
4.3	Class Distribution in VIS Drone . . . . .	30
4.4	Performance comparison of MAMT and EMAMT on mAP at 50% IoU threshold (left) and the average mAP across IoU thresholds from 50% to 95% (right) for the COCO2017 dataset . . . . .	37
4.5	Performance comparison of MAMT and EMAMT on mAP at 50% IoU threshold (left) and the average mAP across IoU thresholds from 50% to 95% (right) for the UAV-SOD dataset . . . . .	38
4.6	Performance comparison of MAMT and EMAMT on mAP at 50% IoU threshold (left) and the average mAP across IoU thresholds from 50% to 95% (right) for the VisDrone dataset . . . . .	39

# List of Tables

3.1	Comparison of Object Detection Models Sorted by Number of Parameters	26
4.1	Basic statistics of COCO dataset bounding boxes . . . . .	28
4.2	Basic statistics of UAV-SOD dataset bounding boxes . . . . .	29
4.3	Basic statistics of VisDrone dataset bounding boxes . . . . .	30
4.4	Details of training parameters per dataset . . . . .	35
4.5	Results of training for COCO dataset . . . . .	36
4.6	Results of training for UAV-SOD dataset . . . . .	37
4.7	Results of training for VisDrone dataset . . . . .	38

# 1 Introduction

Remote sensing imaging is a process used to gather information about objects or areas from a distance, typically using aircraft or satellites. This process is essential in various fields due to its ability to detect and monitor the physical characteristics of an area by measuring its reflected and emitted radiation.

Remote sensing imaging starts with data acquisition through sensors, that are mounted on platforms like satellites or aircraft, capture electromagnetic radiation and can range from simple cameras to complex radar systems. After capturing this data, it is transmitted to ground stations for processing. The processing stage often involves correcting any image distortions, enhancing details, and converting the raw data into usable formats.

Remote sensing imaging has applications across a broad spectrum of fields. Starting with environmental monitoring is one of the primary uses, enabling the observation and analysis of environmental changes like deforestation and the health of aquatic ecosystems. In agriculture, it helps monitor crop health and soil conditions, aiding in the efficient management of resources. The technique is also crucial in disaster management, where it is used to assess damage from natural disasters and plan effective responses. Urban planning benefits from remote sensing by providing data for the development and monitoring of infrastructure and urban growth. In the military and intelligence sectors, remote sensing is key for surveillance and reconnaissance, providing critical information for national security.

Provided the numerous applications of remote sensing images, the computer vision research community is continually pushing to develop object detection models that can effectively parse and interpret the vast amount of data captured by remote sensors. In remote sensing images the objects are small fraction of the pixels of the image, qualifying this process as Small Object Detection.

Even though impressive results have been achieved on large and medium objects in large-scale detection benchmarks, the performance on small or tiny objects is far from satisfactory. Compared with large and medium objects, the small objects are more difficult to detect accurately, because of four main difficulties. Firstly, small objects have low resolution and insufficient features. Secondly, the span of object-scale is large and multiple scales coexist. Thirdly, the examples of small objects are scarce and lastly the categories for small objects are imbalanced for the majority of datasets. The concept of small or tiny objects seeks to elucidate the scale of these objects or the proportion of pixels they occupy within the entire image. There are two main ways to define small objects.

The first way is the use relative size. According to the Krishna and Jawahar [2] showed that an object is considered small if it occupies only a tiny portion of the image, which is less than 1% of the image area. Namely, the bounding box of a small object should cover less than 1% of the original image. The second way of defining a small object by using the absolute size, where a small object has size less than 32x32 pixels defined in MS-COCO dataset or 16x16 pixels defined in USC-GRAD- STDdb [22].

There have been some improvements of the models using different techniques, but all these improvements come at a increased complexity and size of the model. This complexity can be prohibitive for applications in a satellite or an Unmanned Aerial Vehicle since their computation capabilities are limited. Driven by the need for more precise object detection models, this thesis proposes a novel methodology to reduce the computation cost of the detection model for utilization in such cases.

This thesis aims to explore the combination of two successful models from two different approaches in object detection, while maintaining a smaller model size. The evaluation process utilizes datasets that have been parts of employed in the original research papers of these models. Furthermore, this thesis extends its scope to the field of Remote Sensing Images (RSI). Both the original and modified versions of the models will be evaluated using a common RSI dataset. This will facilitate a comprehensive comparison of all model results within a consistent dataset, thereby providing valuable insights into their performance in real-world scenarios.

The remainder of the thesis is organized as follows:

Chapter 2 contains related work surrounding the scope of the thesis. It starts with an explanation of the architecture of Recurrent Convolutional Neural Networks (R-CNNs) alongside the Feature Pyramid Networks and analyzes the distinct role and functionality of each component. It follows with the explanation of the architecture of the Vision Transformers that were used as a basis for the detector of our model. It continues by explaining the difficulties of detecting small objects in remote sensing images.

Chapter 3 introduces the architecture of the suggested model and is presented, providing an extensive description of its design and functionality. It also highlights the significant publications and research that have been a major help in advancing and improving the model's design.

Chapter 4 offers an in-depth overview of the datasets used to evaluate the proposed model. It states the specific parameters used throughout the training phase to ensure a thorough knowledge of the model's learning process. The experimental findings are presented at the end of the chapter, providing a concrete indicator of the model's effectiveness.

Chapter 5 analyzes the experimental findings and discuss the implications of the differences that were observed across different models and datasets. This aims to unravel the underlying implications of these differences, thereby enhancing the understanding of the models' performance across different datasets.

Chapter 6 provides an overview of the future work which aims at investigating performance differences, enhancing the model's performance and testing the method's generalizability across various datasets and domains.

## 2 Related Work

This chapter highlights the theories and recent advancements in the fields of remote sensing and computer vision, particularly in small object detection. By examining previous research that addresses those challenges, this section not only underscores the technological progress achieved but also identifies the gaps that the current model aims to bridge. In the field of computer vision, Convolutional Neural Networks (CNNs) [18] served as the initial models for image analysis, primarily focused on image classification where the entire image is labeled as a single object category. While CNNs had great performance in these tasks, their application to object detection in complex images revealed significant limitations.

Object detection models can be broadly categorized by annotation method into anchor-based and anchor-free approaches, and by detection method into dense prediction (single-stage) and sparse prediction (multi-stage) techniques. This categorization helps in understanding the diverse strategies employed in detecting objects across different scenarios.

This chapter begins with the foundational R-CNN model, which introduced the use of convolutional networks for robust object detection. The following sections dive into Fast R-CNN and Faster R-CNN, which iteratively refined the integration of region proposal mechanisms with deep learning, significantly enhancing detection efficiency and speed. The exploration continues with Mask R-CNN and Feature Pyramid Networks, which extended capabilities to instance segmentation and improved feature representation at multiple scales, respectively.

Single-stage detection models, or dense prediction models, such as YOLO (You Only Look Once) and SSD (Single Shot MultiBox Detector), streamline the detection process by eliminating the need for a separate region proposal step. These models directly predict object classes and bounding box coordinates from full images in one evaluation, optimizing for speed and efficiency.

The latter sections of the chapter explore cutting-edge developments like the Vision Transformer and Masked-Attention Mask Transformer, which incorporate transformer architectures to push the boundaries of object detection and segmentation.

### 2.1 Multi-stage Object Detection Models

Multi-stage object detection models involve a more complex process that typically includes distinct phases for generating region proposals and then classifying these proposals into specific object categories. These models first isolate potential object locations before applying sophisticated classification and bounding box regression techniques. This separation allows for more precise detections and higher overall accuracy, making multi-stage models adept at handling complex image scenarios with multiple objects and varying scales. The trade-off, however, is usually slower processing speeds compared to single-stage detectors.

### 2.1.1 Region-based Convolution Neural Networks

The R-CNN family of models represents a fundamental shift in object detection, introducing deep learning to generate high-quality region proposals that are then classified by a convolutional neural network. This evolutionary path not only streamlined the detection pipeline but also improved the scalability and applicability of these models in real-world scenarios, where speed and accuracy are crucial. The successive refinements from R-CNN through Mask R-CNN highlight a trajectory of continuous improvement, with each iteration bringing more sophisticated integration of features and functionalities.

#### Region-based Convolution Neural Networks

The need for more sophisticated solutions that could accurately identify and locate multiple objects within images led to the development of Region-based Convolutional Networks (R-CNNs) [12]. Starting with the base Region-based Convolution Neural Network This approach combines region proposal algorithms with the feature extraction capabilities of CNNs. R-CNNs begin by generating potential object-bound regions in an image, a process known as region proposal. Each region is then cropped and resized to a fixed size before being fed into a pre-trained convolutional neural network.

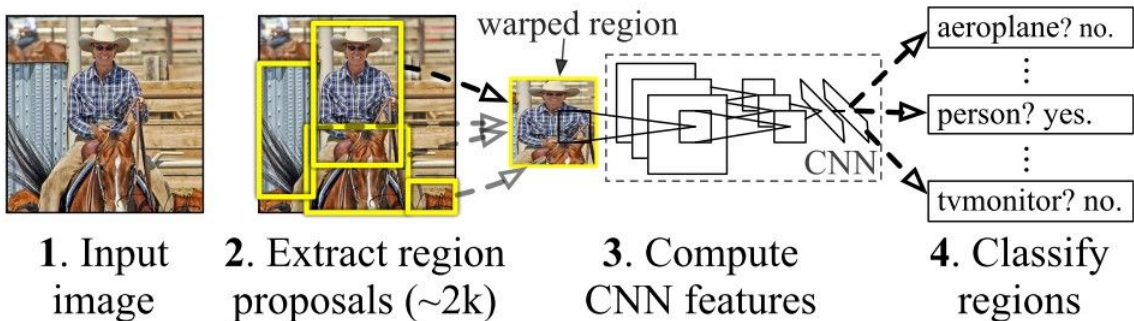


Figure 2.1: Region-based Convolution Neural Network Architecture [12]

As presented in the 2.1 the R-CNN consists of 3 main modules. The first module generates 2,000 region proposals using the Selective Search algorithm. After being resized to a fixed pre-defined size, the second module extracts a feature vector of length 4,096 from each region proposal. The third module uses a pre-trained SVM algorithm to classify the region proposal to either the background or one of the object classes.

Some the limitations of the R-CNN model are the facts that it is a multi-stage model, where each stage is an independent component, thus, it cannot be trained end-to-end. Also the R-CNN depends on the Selective Search algorithm for generating region proposals, which takes a lot of time and cannot be customized to the detection problem. Lastly each region proposal is fed independently to the CNN for feature extraction, which makes it impossible to run R-CNN in real-time.

## Fast Region-based Convolution Neural Networks

Fast R-CNN [11] improved upon the original R-CNN's efficiency, where instead of cropping and resizing each region separately, the entire image is passed through the CNN to extract features. Regions of interest (ROIs) are then selected from the feature map using the proposed bounding boxes from the selective search. These ROIs are then pooled into a fixed-size feature map and passed through fully connected layers for classification and bounding box regression in the figure 2.2.

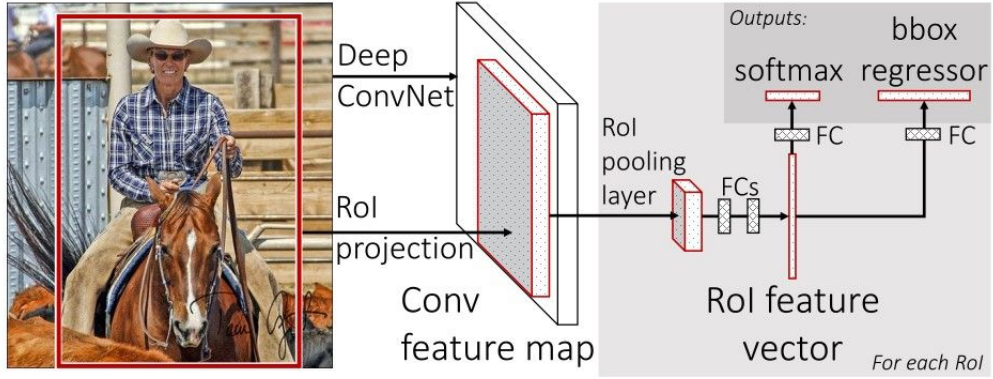


Figure 2.2: Fast Region-based Convolution Neural Network Architecture [11]

In this model a proposed a new layer called ROI Pooling that extracts equal-length feature vectors from all proposals in the same image, where compared to R-CNN, which has multiple stages, Faster R-CNN builds a network that has only a single stage.

The ROI pooling layer uses max pooling to convert the features inside any valid region of interest into a small feature map with a fixed spatial extent of  $H \times W$ , where  $H$  and  $W$  are layer hyper-parameters that are independent of any particular ROI. In this paper, an ROI is a rectangular window into a convolution feature map. Each ROI is defined by a four-tuple  $(r, c, h, w)$  that specifies its top-left corner  $(r, c)$  and its height and width  $(h, w)$ . Also one of the great inclusions of this model was the implementation of multi-task loss:

$$L(p, u, t', v) = L_{cls}(p, u) + \lambda[u \geq 1]L_{loc}(t', v)z \quad (1)$$

,where the classification loss  $L_{cls}(p, u)$  is defined as the negative log likelihood of the true class  $u$ , expressed as:

$$L_{cls}(p, u) = -\log p_u \quad (2)$$

The localization loss  $L_{loc}$  is defined over the predicted bounding box parameters  $t' = (t'_x, t'_y, t'_w, t'_h)$  and the ground truth bounding box parameters  $v = (v_x, v_y, v_w, v_h)$  for class  $u$ . The Iverson bracket  $[u \geq 1]$  is used as an indicator function that evaluates to 1 when  $u$  is 1 or more, and 0 otherwise. This function helps in applying the localization loss only when there is a foreground class detected, effectively ignoring the background.

The overall loss  $L(p, u, t', v)$  is then a combination of classification and localization losses, modulated by a parameter  $\lambda$ , representing the trade-off between these two tasks:

$$L(p, u, t', v) = L_{cls}(p, u) + \lambda[u \geq 1]L_{loc}(t', v) \quad (3)$$

## Faster Region-based Convolution Neural Networks

While Fast R-CNN improved upon its predecessors in terms of both speed and accuracy, the Faster R-CNN architecture [23] emerged as an even more refined version. Fast R-CNN effectively addressed the inefficiencies of previous models by integrating a region of interest (RoI) pooling layer to connect convolutional feature extraction and region proposal tasks. However, it still relied on external region proposal algorithms, which remained a bottleneck in terms of computational efficiency and speed.

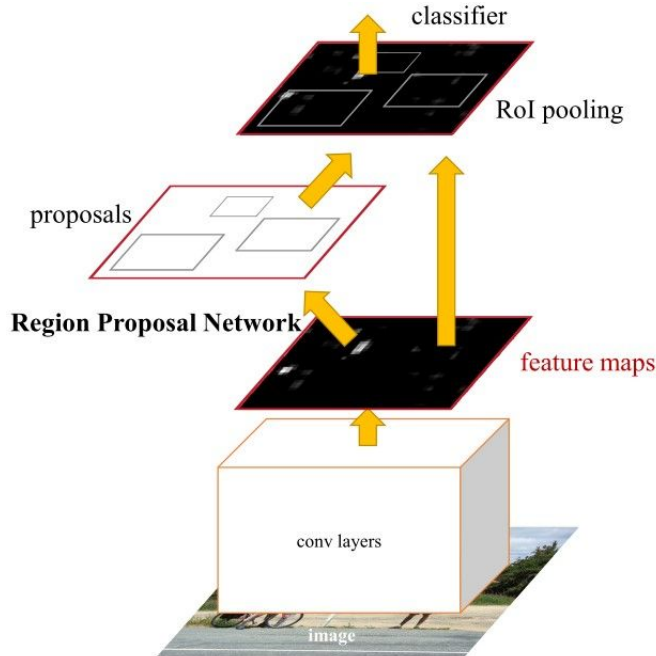


Figure 2.3: Faster Region-based Convolution Neural Network Architecture [23]

Faster R-CNN resolved this by introducing a novel component, the Region Proposal Network (RPN). A Region Proposal Network takes an image (of any size) as input and outputs a set of rectangular object proposals, each with an objectness score. This process is modeled with a fully convolutional network, because the ultimate goal is to share its computation with a Fast R-CNN object detection network, as it is assumed that both nets share a common set of convolutional layers, as seen in the Figure 2.3.

To generate region proposals, a small network slides over the convolutional feature map output by the last shared convolutional layer. This small network takes as input an  $n \times n$  spatial window of the input convolutional feature map. Each sliding window is mapped to a lower-dimensional feature. This feature is fed into two sibling fully-connected layers—a box-regression layer (reg layer) and a box-classification layer (cls layer). This mini-network is illustrated at a single position in the Figure 2.4. Also since the mini-network operates in a sliding-window fashion, the fully-connected layers are shared across all spatial locations.

This architecture is naturally implemented with an  $n \times n$  convolutional layer followed by two sibling  $1 \times 1$  convolutional layers.

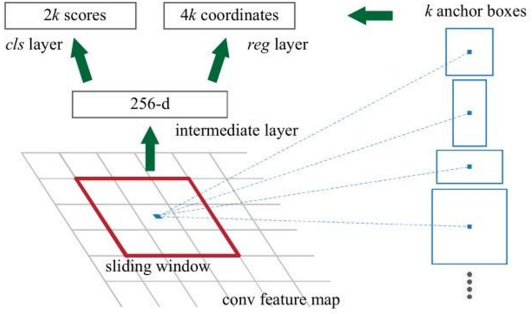


Figure 2.4: Region Proposal Network [23]

At each sliding-window location, there is simultaneously a prediction of multiple region proposals, where the number of maximum possible proposals for each location is denoted as  $k$ . The  $k$  proposals are parameterized relative to  $k$  reference boxes, which are called anchors. An anchor is centered at the sliding window in question, and is associated with a scale and aspect ratio as seen again in Figure 2.4. By default 3 scales and 3 aspect ratios are used, yielding  $k = 9$  anchors at each sliding position. For a convolutional feature map of a size  $W \times H$ , there are  $W \times H \times k$  anchors in total.

### Masked Region-based Convolution Neural Networks

Mask R-CNN [13] builds on the ideas and successes of the Faster R-CNN model, which predicts both a class label and a bounding-box offset for each candidate object. To these, Mask R-CNN adds a third branch specifically designed to output the object mask, providing a straightforward and logical extension to the existing framework. This addition allows Mask R-CNN to capture the precise spatial layout of objects, a task that necessitates extracting significantly finer detail than what is required for classifying objects or predicting bounding boxes alone.

Mask R-CNN adopts the same two-stage procedure as Faster R-CNN, with an identical first stage the RPN. In the second stage, in parallel to predicting the class and box offset, Mask R-CNN also outputs a binary mask for each ROI. This is in contrast to most recent systems, where classification depends on mask predictions. This approach follows the spirit of Fast R-CNN that applies bounding-box classification and regression in parallel.

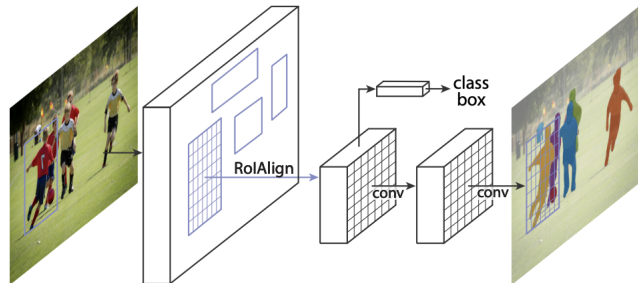


Figure 2.5: Mask Region Convolution Neural Network Architecture [13]

A mask encodes an input object’s spatial layout. Thus, unlike class labels or box offsets that are inevitably collapsed into short output vectors by fully-connected layers, extracting the spatial structure of masks can be addressed naturally by the pixel-to-pixel correspondence provided by convolutions. Specifically, an  $m \times m$  mask is predicted from each ROI using an FCN. This allows each layer in the mask branch to maintain the explicit  $m \times m$  object spatial layout without collapsing it into a vector representation that lacks spatial dimensions. Unlike previous methods that resort to fully-connected layers for mask prediction, this fully convolutional representation requires fewer parameters, and is more accurate as demonstrated by experiments.

This pixel-to-pixel behavior requires our ROI features, which themselves are small feature maps, to be well aligned to faithfully preserve the explicit per-pixel spatial correspondence. This motivated us to develop the following ROIAlign layer that plays a key role in mask prediction.

RoIPool is a standard operation for extracting a small feature map like  $7 \times 7$  from each ROI. RoIPool first quantizes a floating-number ROI to the discrete granularity of the feature map, this quantized ROI is then subdivided into spatial bins which are themselves quantized, and finally feature values covered by each bin are aggregated usually by max pooling.

Quantization, such as that performed on a continuous coordinate  $x$  by calculating  $\frac{x}{16}$ , where 16 represents the feature map stride accompanied by the rounding. Similarly, this quantization process occurs when coordinates are divided into discrete bins, for example, into a  $7 \times 7$  grid. However, these quantization steps can lead to slight misalignments between the Region of Interest (ROI) and the features extracted from it, potentially affecting the accuracy of the model.

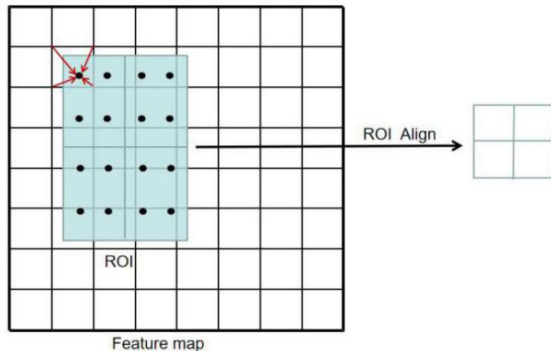


Figure 2.6: Mask Region Of [13]

While this may not impact classification, which is robust to small translations, it has a large negative effect on predicting pixel-accurate masks. To address this, a ROIAlign layer is proposed that removes the harsh quantization of RoIPool, properly aligning the extracted features with the input. A bilinear interpolation is used to compute the exact values of the input features at four regularly sampled locations in each ROI bin, and aggregate the result.

Furthermore once again this model utilizes a multi-task loss in order to take into consideration all the outputs of the model.

$$L = L_{cls} + L_{box} + L_{mask} \quad (4)$$

The mask branch has a  $K \times m^2$ -dimensional output for each ROI, which encodes

$K$  binary masks of resolution  $m \times m$ , one for each of the  $K$  classes. To this a per-pixel sigmoid is applied, and define  $L_{mask}$  as the average binary cross-entropy loss. For an ROI associated with ground-truth class  $k$ ,  $L_{mask}$  is only defined on the  $k$ -th mask. This definition of  $L_{mask}$  allows the network to generate masks for every class without competition among classes, since on the dedicated classification branch to predict the class label used to select the output mask. This decouples mask and class prediction. This is different from common practice when applying FCNs to semantic segmentation, which typically uses a per-pixel softmax and a multinomial cross-entropy loss. In that case, masks across classes compete; in our case, with a per-pixel sigmoid and a binary loss, they do not.

### 2.1.2 Feature Pyramid Networks

The concept of Feature Pyramid Networks (FPNs) was a significant advancement in object detection and segmentation, by leveraging the inherent multi-scale, pyramidal hierarchy of deep convolutional networks. The first subsection details the basic Feature Pyramid Network, an architecture that efficiently creates a pyramid of features at multiple levels, enabling the detection of objects at various scales with improved accuracy. This structure uses a top-down approach with lateral connections to combine low-resolution, semantically strong features with high-resolution, semantically weaker features, enhancing the network’s ability to detect objects across different scales. The subsequent subsection explores the Extended Feature Pyramid Network, which builds upon the original FPN by introducing enhancements that further refine feature integration and improve detection performance, particularly in challenging scenarios with complex object orientations and scales.

#### Feature Pyramid Network

With Feature Pyramid Networks [16] the objective is to harness the pyramidal feature hierarchy of a Convolutional Networks, which inherently contains semantic information from low to high levels, to construct a feature pyramid that maintains high-level semantics throughout. The method processes a single-scale image of arbitrary size and produces proportionally sized feature maps at multiple levels, utilizing a fully convolutional approach. This procedure is compatible with various backbone convolutional architectures, and this paper demonstrates results using ResNets. The construction of the pyramid incorporates a bottom-up pathway, a top-down pathway, and lateral connections, which are detailed below and seen in the Figure 2.7.

The bottom-up pathway is the feed forward computation of the ConvNet backbone, which computes a feature hierarchy consisting of feature maps at several scales with a scaling step of 2. There are often many layers producing output maps of the same size and these layers are in the same network stage. For the feature pyramid, one pyramid level for each stage is defined. The output of the last layer of each stage is chosen as the reference set of feature maps, which will be enriched to create the pyramid. This choice is logical because the deepest layer of each stage is expected to have the strongest features.

Specifically, for ResNets, the feature activations output by the last residual block of each stage are utilized. These outputs are denoted as  $C2, C3, C4, C5$  corresponding to the outputs of conv2, conv3, conv4, and conv5, respectively. It is important to note that these have strides of 4, 8, 16, 32 pixels with respect to the input image. The conv1 output is not included in the pyramid due to its large memory footprint.

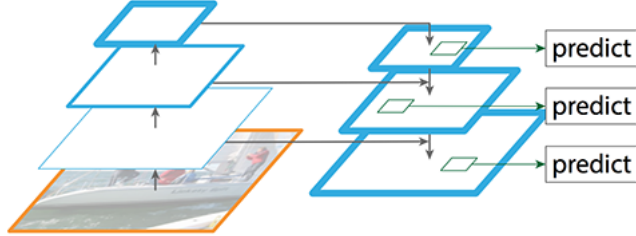


Figure 2.7: Feature Pyramid Network [16]

The top-down pathway hallucinates higher resolution features by up-sampling spatially coarser, but semantically stronger, feature maps from higher pyramid levels. These features are then enhanced with features from the bottom-up pathway via lateral connections. Each lateral connection merges feature maps of the same spatial size from the bottom-up pathway and the top-down pathway. The bottom-up feature map is of lower-level semantics, but its activations are more accurately localized as it was sub-sampled fewer times. With a coarser-resolution feature map, the spatial resolution is up-sampled by a factor of 2. The up-sampled map is then merged with the corresponding bottom-up map (which undergoes a  $1 \times 1$  convolutional layer to reduce channel dimensions) by element-wise addition as seen in the figure 2.8. This process is iterated until the finest resolution map is generated. To start the iteration, simply attach a  $1 \times 1$  convolutional layer on  $C_5$  to produce the coarsest resolution map.

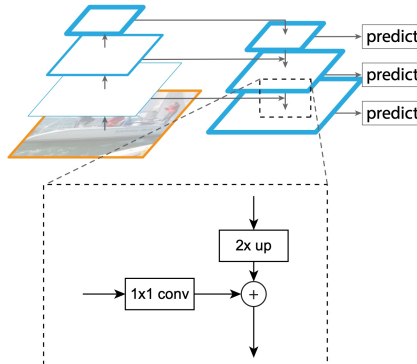


Figure 2.8: Feature Pyramid Network Top-Down path [16]

Finally a  $3 \times 3$  convolution is added on each merged map to generate the final feature map, which is to reduce the aliasing effect of up-sampling. This final set of feature maps is called  $P_2, P_3, P_4, P_5$ , corresponding to  $C_2, C_3, C_4, C_5$  that are respectively of the same spatial sizes. Since all levels of the pyramid use shared classifiers/regressors as in a traditional featurized image pyramid, a fixed feature dimension or numbers of channels is set, with the value being denoted as  $d$  in all the feature maps. With  $d = 256$  in this paper and thus all extra convolutional layers have 256-channel outputs. Simplicity is central to this design and it has been proven that this model is robust to many design choices. Experiments with more sophisticated blocks have been made and observed marginally better results.

### 2.1.3 Vision Transformers

The Vision Transformer (ViT) [9] model represents a significant shift in the approach to image recognition, applying architectures originally developed for natural language processing (NLP) to computer vision tasks. The ViT moves away from traditional convolutional neural networks (CNNs) to embrace transformers, a model type that leverages self-attention mechanisms originally designed for text data. Like NLP systems, ViT treats an image as a sequence of fixed-size patches, akin to words in a sentence, and processes these patches through a series of transformer layers to capture complex inter-patch relationships and contextual information.

In a transformer model for NLP, the encoder processes the input text by mapping it into a high-dimensional space to capture contextual relationships, while the decoder generates the output text sequentially, using the encoder's context-rich representations along with its own input to predict the next word or sequence, thereby facilitating tasks like translation, summarization, and text generation. The architecture of a transformer model can be seen in the figure 2.9, where the left part is the transformer encoder and the right part is the decoder.

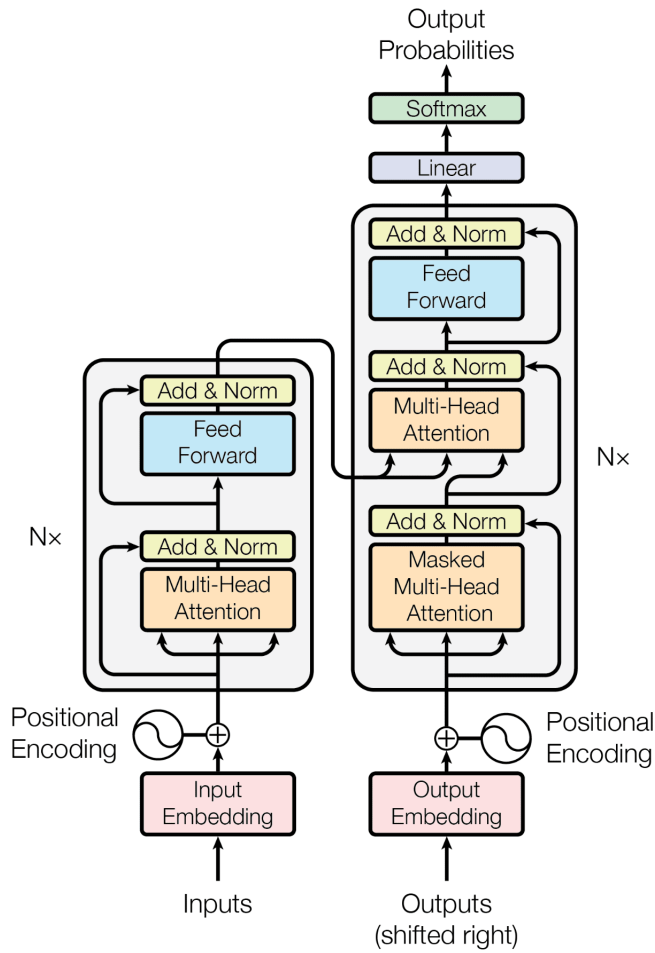


Figure 2.9: NLP Transformer Architecture [9]

On the other hand, the ViT encoder processes the input image, which is divided into patches and linearly embedded. The encoder’s self-attention mechanism allows the model to consider each patch in the context of others, capturing the global context of the image. This is crucial for tasks like image classification or object detection, where understanding the entire image context is important. The encoder is responsible for understanding the content and context of the image, learning to identify features and patterns relevant to the task at hand. Furthermore ViTs typically do not use a decoder because their primary tasks do not involve generating sequential data as is the case in machine translation or text generation in NLP. Instead, the output of the ViT encoder is directly connected to task-specific heads like linear layers for classification or additional layers for object detection that interpret the encoder’s representations to make predictions.

In the pre-transformer encoder stage of processing an image, the initial input, typically of size  $H \times W \times D$  (height, width, depth), is segmented into  $N$  non-overlapping patches. Each patch has dimensions  $P \times P \times D$  and is extracted in a grid-like pattern across the image. These patches are then flattened and undergo a linear projection to transform them into a higher-dimensional space, with each patch represented as a one-dimensional array. To ensure that spatial information is not lost during this transformation, positional encodings of the same dimension,  $D'$ , are added to these patch embeddings. This results in each patch embedding maintaining a sequence of vectors, each with dimension  $D'$ . The linear projection itself is facilitated by a learnable matrix that the flattened patches are multiplied with, culminating in an array of size  $N \times D'$ , where each row represents the embedded representation of a patch. This structured approach allows the model to retain a detailed understanding of the original image’s spatial layout as it processes through the transformer encoder.

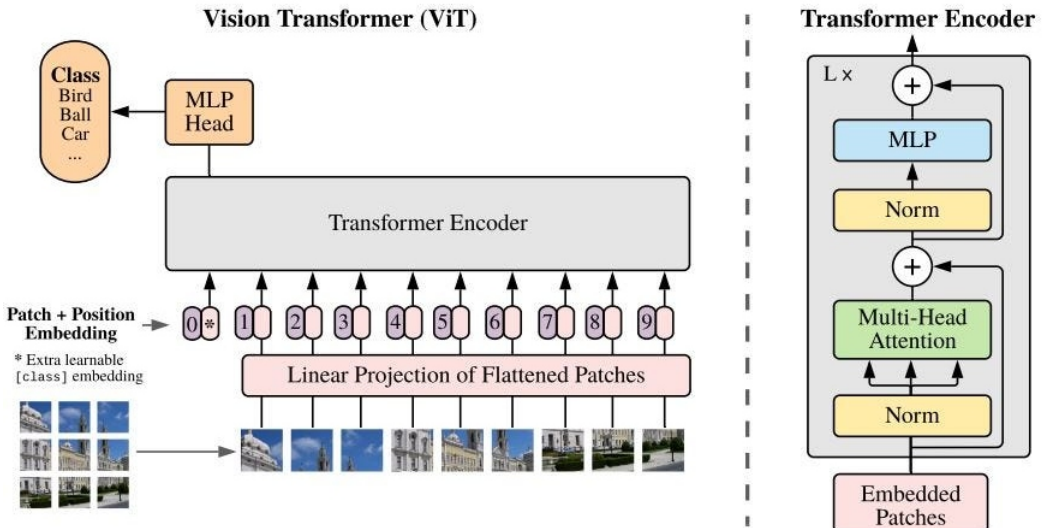


Figure 2.10: Vision Transformer Architecture [9]

The transformer encoder in image processing is composed of several transformer blocks arranged in sequence, each designed to refine the representation of image patches through a series of specialized sub-components. Each block starts with Layer Normalization, which is applied before self-attention and MLP operations to stabilize the training process and facilitate model convergence. Unlike batch normalization, layer normalization is preferred in transformers as they handle sequential data, ensuring that the size of the data remains at  $N \times D'$ .

Following normalization, the Multi-Head Self-Attention (MHA) mechanism is used, accepting queries, keys, and values as inputs. This allows the model to simultaneously focus on different parts of the image, enhancing the contextual understanding of the image by computing attention scores and updating embeddings without altering the initial data size of  $N \times D'$ .

Residual Connections are employed after MHA and MLP within each transformer block, where the input to the block is added back to its output. This practice helps preserve information across the layers, combating the vanishing gradient problem and facilitating deeper model architectures by improving gradient flow.

Additionally, each block contains an MLP (Multi-Layer Perceptron) segment, which includes fully connected layers featuring a GELU activation function and often incorporates dropout to prevent overfitting. This component further processes the output of the self-attention mechanism before it passes through another round of residual connections. The cumulative effect of these operations in each transformer block is to continuously refine the embeddings, with the input and output of each block being arrays of size  $N \times D'$ , effectively updating the representation at each step of the sequence.

In the post-transformer encoder phase of image processing, several critical modules refine the processed features for specific tasks such as object detection and classification. The MLP Head is employed immediately after the transformer encoder to project the encoded features into a lower-dimensional space that is more suitable for object detection tasks. The dimensionality of the MLP head's output varies depending on its architecture and the specifics of the object detection task being performed, adapting the complex, high-dimensional data into a form that can be effectively used for the subsequent steps.

## 2.2 Single-stage Object Detection Models

Single-stage object detection models represent a streamlined approach to identifying and localizing objects within an image. Unlike multi-stage models, single-stage models, such as YOLO (You Only Look Once) and SSD (Single Shot MultiBox Detector), operate in a direct manner by predicting object classes and bounding box coordinates in a single forward pass through the network. This methodology not only simplifies the detection pipeline but also enhances the speed of detection, making single-stage models particularly well-suited for real-time applications. However, this increase in speed can sometimes come at the cost of lower accuracy, especially in detecting small or overlapping objects.

### 2.2.1 You Only Look Once

YOLO (You Only Look Once) [21] represents a shift in object detection techniques through its simple and highly efficient approach. Unlike traditional object detection methods that involve a multi-step process, YOLO employs a single convolutional network that simultaneously predicts multiple bounding boxes and class probabilities for those boxes. This process is followed by a non-maximum suppression step to finalize the detections. The architecture is based on a standard high-quality image classification network truncated before any classification layers, known as the base network, which is then augmented with additional layers to detect objects at multiple scales.

One of the primary benefits of YOLO is its speed, achieving real-time processing rates of up to 45 frames per second on a Titan X GPU, and a fast version that exceeds 150 fps. This capability allows YOLO to handle streaming video in real-time with close to no latency, significantly outperforming other real-time systems in mean average precision. Moreover, YOLO reasons globally about the image during both training and testing phases, which helps it encode contextual information about object classes and their appearances. This global perspective reduces background errors significantly compared to methods like Fast R-CNN, which often misclassify background patches as objects.

In addition, YOLO learns generalizable representations of objects, demonstrated by its superior performance when trained on natural images and tested on artwork, outperforming other top detection methods. However, while YOLO excels in identification speed and generalizability, it sometimes struggles with precisely localizing objects, particularly small ones.

The network divides the input image into an  $S \times S$  grid, with each grid cell responsible for detecting objects whose centers fall within the cell. Each cell predicts multiple bounding boxes and confidence scores, which reflect the presence and accuracy of object detection. These predictions are based on the intersection over union (IOU) metric between the predicted boxes and ground truth.

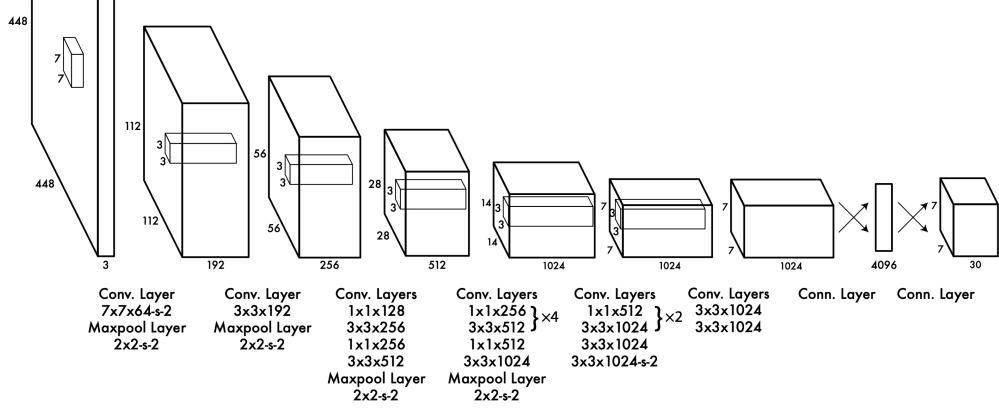


Figure 2.11: YOLO Architecture [21]

The convolutional neural network of YOLO, inspired by the GoogLeNet model for image classification, comprises 24 convolutional layers followed by 2 fully connected layers. This structure utilizes  $1 \times 1$  reduction layers followed by  $3 \times 3$  convolutional layers to efficiently predict bounding boxes and class probabilities. Despite its strengths, YOLO imposes certain spatial constraints on bounding box predictions due to each grid cell predicting only two boxes and one class, which can limit its effectiveness in scenarios with small or clustered objects. Additionally, YOLO's simpler architecture struggles with unusual object aspect ratios and configurations and is less forgiving of localization errors in smaller bounding boxes due to its coarse feature predictions and the uniform treatment of errors across all box sizes in its loss function.

In conclusion, YOLO's innovative approach integrates the components of object detection into a single neural network, leveraging features from the entire image to make global predictions about all objects present. This end-to-end training capability and real-time processing speed maintain high average precision, making YOLO a groundbreaking model in the field of object detection, despite some challenges with small and closely spaced objects.

## 2.2.2 Single Shot MultiBox Detector

The Single Shot MultiBox Detector (SSD) [17] employs a streamlined architecture that integrates detection and classification into a single pass through a feed-forward convolutional network, thereby enhancing speed without compromising accuracy. This model produces a fixed collection of bounding boxes and class scores for each object instance identified, followed by a non-maximum suppression step to finalize the detections. The foundation of SSD is a base network derived from standard high-quality image classification architectures, which is truncated before any classification layers.

To adapt this base network for object detection, SSD incorporates multiple convolutional feature layers at the end of the network. These additional layers decrease progressively in size, allowing for the detection of objects at various scales—a notable improvement over models like Overfeat and YOLO, which are limited to single scale feature maps. Each feature layer in SSD employs a unique set of convolutional filters to predict detection outcomes at that scale, thus enhancing the model’s responsiveness to objects of varying dimensions as seen in the Figure 2.12.

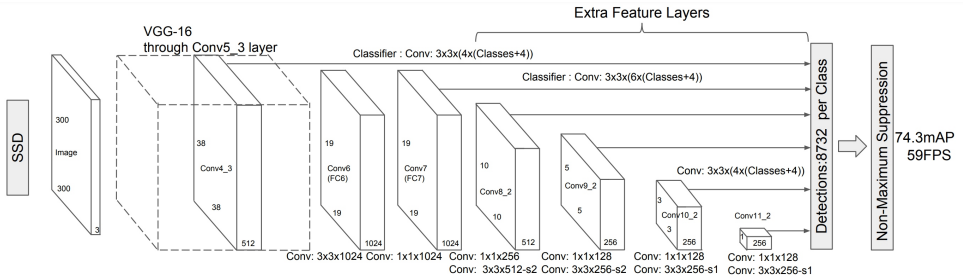


Figure 2.12: Single Shot MultiBox Detector Architecture [17]

SSD further refines its detection capabilities through the use of convolutional predictors at each feature layer. These predictors apply a  $3 \times 3 \times p$  convolutional kernel to each feature map location, generating scores for category presence or box shape offsets relative to predefined default boxes. These default boxes, similar to the anchor boxes used in Faster R-CNN but applied across multiple resolutions, are associated with each feature map cell. For each default box, the model computes class scores and spatial offsets, improving detection precision. This mechanism results in an extensive set of outputs for each feature map cell, ensuring robust detection across a diverse array of object types and sizes.

# 3 Methodology

In our exploration of various object detection architectures, it became clear that single-stage detector models, while notable for their efficiency, did not meet the accuracy demands required for small object detection. Given the challenges associated with detecting smaller objects, we considered multi-stage models as a more viable solution, because these models are known for their enhanced precision and adeptness at handling intricate detection tasks. Through our research, a potential model combination emerged as a great candidate. The Feature Pyramid Network family of models excels in multi-scale representation essential for resolving objects of varying sizes, while the Vision Transformers family provides an exceptional ability to grasp global contextual dependencies within images through the attention modules.

By integrating these models, as a backbone and a detector we found that we can leverage the complementary strengths of both frameworks, thus creating a robust multi-stage model specifically made to achieve the best possible results in small object detection.

## 3.1 Architecture

Choosing a multi-stage model for small object detection does not necessarily imply that the model will be demanding in terms of trainable parameters or challenging to train. Our approach strategically combines the two types of models in order to harness their individual strengths while maintaining manageable complexity and training efficiency. This integration ensures that our multi-stage detector not only achieves an elevated accuracy but also remains practical in terms of computational resources and training time, making it a viable solution for real-world applications where both performance and efficiency are critical.

In this section we are going to describe and explain the model we developed in detail with the aim of successfully tackling the Small Object Detection challenge. The model we created is named Extended Masked-Attention Mask Transformer, a name based on the models we decided to integrate being the Extended Feature Pyramid Network [8] and the Masked-Attention Mask Transformer (MAMT) [5].

A very interesting finding in the EFPN article is that over the past years, rapid development of deep learning has boosted the popularity of CNN-based detectors and the improved overall accuracy and efficiency. Unfortunately they still perform poorly when detecting small objects with a few pixels. Since CNN uses pooling layers repeatedly to extract advanced semantics, the pixels of small objects can be filtered out during the down-sampling process.

Utilization of low-level features is one way to pick up information about small objects. The FPN is the first method to enhance features by fusing features from different levels and constructing feature pyramids, where upper feature maps are responsible for larger object detection, and lower feature maps are responsible for smaller object detection. Despite FPN's improvement multi-scale detection performance, the heuristic mapping mechanism between pyramid level and proposal size in FPN detectors may confuse small object detection, since small-sized objects must share the same feature map with medium-sized objects and some large-sized objects.

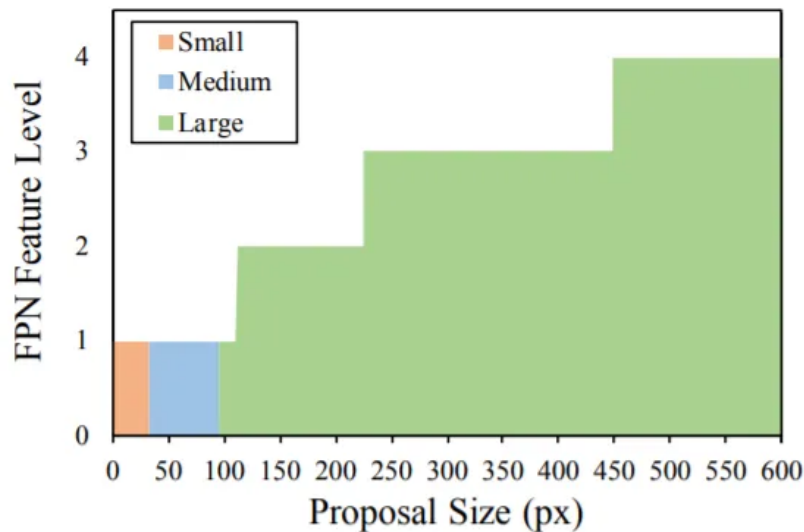


Figure 3.1: Small Object Detection Mapping [8]

### 3.1.1 Extended Feature Pyramid Network

The implementation of the Extended Feature Pyramid follows closely an FPN-like framework embedded with a feature Super Resolution (SR) [1] module. This pipeline directly generates high resolution features from low-resolution images to support small object detection, while stays in low computational cost. The top four pyramid layers are constructed by top-down pathways for medium and large object detection.

The bottom extension of the EFPN contains the very important FTT module, the top-down pathway and the purple pyramid layer in 3.2, that aims to capture regional details for small objects. More specifically, in the extension, the third and fourth pyramid layers of EFPN which are denoted by green and yellow layers respectively in 3.2, are mixed up in the feature super resolution module, the FTT with the aim of producing the intermediate feature  $P'_3$  with selected regional information, which is denoted by a blue diamond in Figure 3.2. Finally the top-down pathway merges  $P'_3$  with a tailor-made high-resolution CNN feature map  $C'2$ , producing the final extended pyramid layer  $P'2$ .

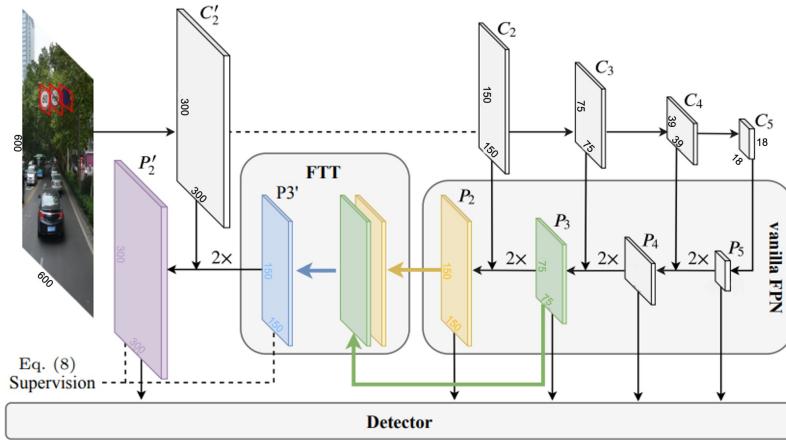


Figure 3.2: Extended Feature Pyramid Network [8]

The current Feature Texture Transfer (FTT) output as seen in the figure synthesizes strong semantics in upper low-resolution features and critical local details in lower high-resolution reference features, but discards disturbing noises in reference. As shown in Figure 3.3, the main input of FTT module is the feature map  $P_3$  from the 3rd layer of EFPN, and the reference is the feature map  $P_2$  from the 4th layer of EFPN.

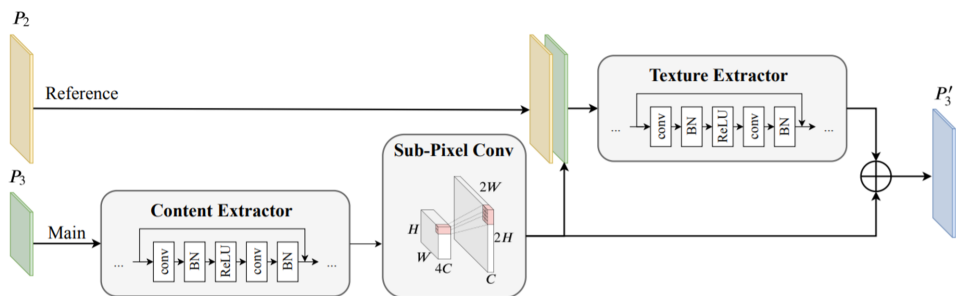


Figure 3.3: Feature Texture Transfer [8]

The output  $P'_3$  can be defined as:

$$P'_3 = E_t(P_2 \| E_c(P_3)_{\uparrow 2}) + E_c(P_3)_{\uparrow 2} \quad (5)$$

,where where  $E_t()$  denotes texture extractor component,  $E_c()$  denotes content extractor component,  $\uparrow 2\times$  here denotes double up-scaling by sub-pixel convolution and  $\kappa$  denotes feature concatenation. The content extractor and texture extractor are both composed of residual blocks. In the main stream, a sub-pixel convolution is applied to upscale spatial resolution of the content features from the main input  $P_3$  considering its efficiency. Sub-pixel convolution augments pixels on the dimensions of width and height via diverting pixels on the dimension of channel.

### 3.1.2 Masked-Attention Mask Transformer

Mask classification architectures group pixels into  $N$  segments by predicting  $N$  binary masks, along with  $N$  corresponding category labels. Mask classification is general enough to address any segmentation or object detection task by assigning different semantics. However, the challenge is to find good representations for each segment. Inspired by DETR [3], each segment in an image can be represented as a  $C$ -dimensional feature vector known as object query and can be processed by a Transformer decoder, trained with a set prediction objective. A simple meta architecture would consist of three components.

A backbone that extracts low resolution features from an image. A pixel decoder that gradually up-samples low-resolution features from the output of the backbone to generate high-resolution per-pixel embeddings. And finally a Transformer decoder that operates on image features to process object queries. The final binary mask predictions are decoded from per-pixel embeddings with object queries. One successful instantiation of such a meta architecture is MaskFormer[4].

Mask2Former adopts this kind meta architecture, with the proposed Transformer decoder in the Figure 3.4 replacing the standard one. The key components of the Transformer decoder include a masked attention operator, which extracts localized features by constraining cross attention to within the foreground region of the predicted mask for each query, instead of attending to the full feature map.

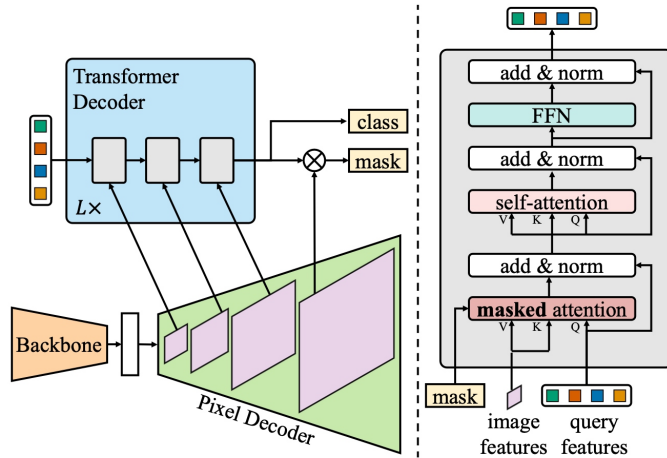


Figure 3.4: Masked-Attention Mask Transformer [5]

To handle small objects, an efficient multi-scale strategy is proposed to utilize high-resolution features. It feeds successive feature maps from the pixel decoder’s feature pyramid into successive Transformer decoder layers in a round robin fashion. Context features have been shown to be important for image segmentation. However, recent studies [10, 14, 24] suggest that the slow convergence of Transformer-based models is due to global context in the cross-attention layer, as it takes many training epochs for cross-attention to learn to attend to localized object regions.

There is the hypothesize that local features are enough to update query features and context information can be gathered through self-attention. For this a masked attention was proposed, a variant of cross attention that only attends within the foreground region of the predicted mask for each query. Standard cross-attention computes:

$$X_l = \text{softmax}(Q_l K_l^T) V_l + X_{l-1} \quad (6)$$

Here,  $l$  is the layer index,  $X_l \in R^{N \times C}$  refers to  $N$   $C$ -dimensional query features at the  $l$ th layer and  $Q_l = f_Q(X_{l-1}) \in R^{N \times C}$ . Here  $X_0$  denotes input query features to the Transformer decoder.  $K_l, V_l \in R^{H_l W_l \times C}$  are the image features under transformation  $f_K()$  and  $f_V()$  respectively, and  $H_l$  and  $W_l$  are the spatial resolution of image features,  $f_Q, f_K$  and  $f_V$  are linear transformations

Our masked attention modulates the attention matrix via:

$$X_l = \text{softmax}(\mathcal{M}_{l-1} + Q_l K_l^T) V_l + X_{l-1} \quad (7)$$

Moreover, the attention mask  $\mathcal{M}_{l-1}$  at feature location  $(x, y)$  is:

$$\mathcal{M}_{l-1}(x, y) = \begin{cases} 0 & \text{if } \mathcal{M}_{l-1}(x, y) = 1 \\ -\infty & \text{otherwise} \end{cases} \quad (8)$$

Here,  $M_{l-1} \in \{0, 1\}^{N \times H_l W_l}$  is the binarized output, thresholded at 0.5 of the resized mask prediction of the previous  $(l-1)$ -th Transformer decoder layer. It is resized to the same resolution of  $K_l$ .  $M_0$  is the binary mask prediction obtained from  $X_0$ , before feeding query features into the Transformer decoder.

High-resolution features improve model performance, especially for small objects [3], however, this is computationally demanding. Thus the solution being an efficient multi-scale strategy to introduce high-resolution features while controlling the increase in computation. Instead of always using the high-resolution feature map, a feature pyramid which consists of both low- and high-resolution features is utilized and feed one resolution of the multi-scale feature to one Transformer decoder layer at a time. Specifically, the feature pyramid produced by the pixel decoder with resolution 1/32, 1/16 and 1/8 of the original image. For each resolution, both a sinusoidal positional embedding  $e_{pos} \in R^{H_l W_l C}$  and a learnable scale-level embedding  $e_{lvl} \in R^{1 \times C}$  is added.

We use those, from lowest-resolution to highest-resolution for the corresponding Transformer decoder layer as shown in Figure 3.4. This is repeated for a 3-layer Transformer decoder  $L$  times. In this case the final Transformer decoder hence has  $3L$  layers.

More specifically, the first three layers receive a feature map of resolution  $H1 = H/32, H2 = H/16, H3 = H/8, W1 = W/32, W2 = W/16, W3 = W/8$ , where  $H$  and  $W$  are the original image resolution. This pattern is repeated in a round robin fashion for all following layers.

### 3.1.3 Extended Masked-Attention Mask Transformer

Throughout our extensive research into advanced object detection models and architectures, it became an interesting idea that a hybrid approach would yield the most effective results, especially for the task of small object detection. The detailed analysis of various architectures led us to the strategic combination of two highly effective models: the Extended Feature Pyramid Network (EFPN) and the Masked-Attention Mask Transformer (MAMT). This integration leverages the EFPN’s robust capability in generating precise multi-scale feature maps and initial bounding boxes and masks with great efficiency, with the MAMT’s advanced attention mechanisms that refine these masks for superior accuracy that is vital for the Small Object Detection task.

In this section we are going to analyze our model, the Extended Masked-Attention Mask Transformer or EMAMT starting with the models architecture in the Figure 3.5.

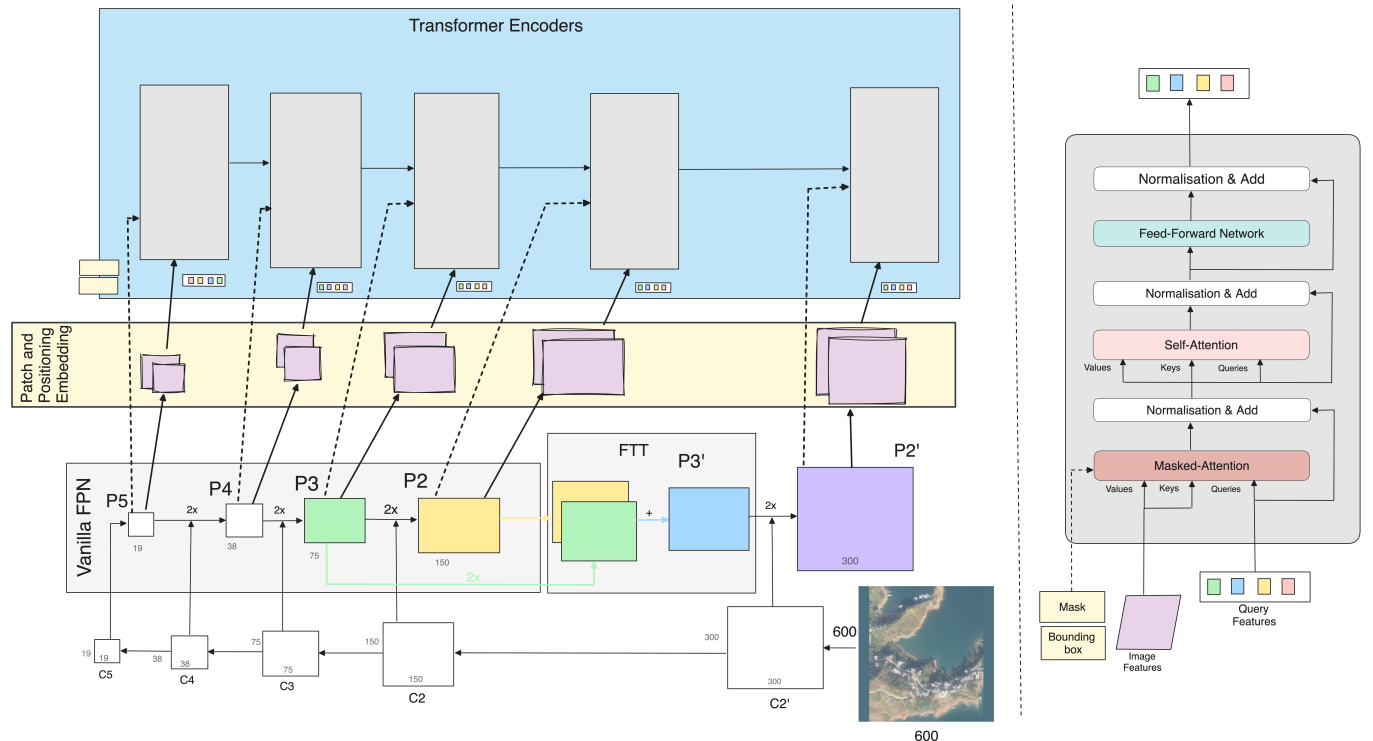


Figure 3.5: Extended Masked-Attention Mask Transformer

Firstly we are going to analyze the EFPN part of the model in the lower left part of the Figure 3.5, where the EFPN model has as a input, an image of size  $600 \times 600$ . The reason for the selection of that size is the backbone we use to generate the rich feature maps for the model. In our architecture we decided that a pre-trained feature extractor that combines great performance and light design was vital. This combination of characteristics led us to the choice of EfficientNet [25] model and more specifically the EfficientNet-B7 model that uses an input size of  $600 \times 600$ . Furthermore we decided to create five feature maps that have the sizes  $(300, 300), (150, 150), (75, 75), (38, 38), (19, 19)$  in order to have a wide range of data for the model to use.

Alongside the feature maps the EFPN also produces the bounding boxes and the initial binary masks that are going to be used by the MAMT detector. The bounding boxes and the masks are implemented on the most detailed feature map  $P'2$  that is the result of the addition of the richest spatial map  $C'2$  and the richest feature map created by the feature

texture transfer  $P'3$ . At the same time we have included a anchor generator model that creates anchors, informed based on the mean and standard deviation of the size of the bounding boxes of each dataset in order to conclude the first cycle of detection, between the actual data, the anchors and the bounding boxes. In this way we are able to train the EFPN model in parallel to the MAMT model, achieving better convergence. With the end of the EFPN model we are expecting a set of five feature maps, a set of bounding boxes and the corresponding classed for each object and the initial binary masks.

The next part of the EMAMT model is the patch and positional embedding we use in order to add to the model the sense of spatial arrangement among the input image patches. Since transformers inherently lack any mechanism to recognize order or position, positional embeddings are crucial for providing this spatial context. The creation of the positional embeddings follows the exact same idea as the original paper of MAMT, since it was the implementation of the sinusoidal positional embedding for images, adapted from the concept originally used in the transformer architecture for natural language processing. This type of embedding generates position encodings based on sine and cosine functions of different frequencies.

At this point we have a set of five embeddings of the feature maps, a set of bounding boxes and the corresponding classes and the binary masks. Along all that information the detector of this model we use a set number of queries that in this case is set to 100, because we wanted to focus on reliable detecting a sensible number of objects. For images that contain more than 100 objects and the annotations we decided to only use the first 100 of them to train the model. Provided all of this data the Vision Transformer architecture can be seen in the Figure 3.6.

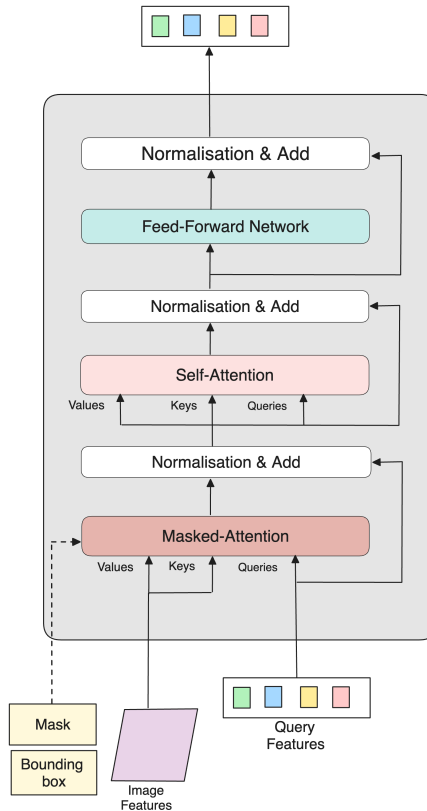


Figure 3.6: Extended Masked-Attention Mask Transformer - Transformer Module

As mentioned in the section 3.1.2 we have the hypothesis that local features are enough to update query features and context information can be gathered through self-attention. For this reason we use masked attention, a variant of cross-attention that only attends within the foreground region of the predicted mask for each query with the aim of better performance and faster convergence. More specifically the masked attention layer is used to focus the model’s attention selectively based on certain predefined or learned criteria like the object queries, typically aligning with relevant areas of the input image. For instance, in tasks like image segmentation, the masked attention layer might concentrate processing on areas within a specific region of interest (ROI), such as the foreground of an image versus the background. This selective attention helps the model to efficiently process only the most informative parts of the image, thereby optimizing computational cost.

Following the masked attention, the cross-attention layer has to integrate additional context or features from another source into the transformer’s workflow. When placed after a masked attention layer, the cross-attention layer can leverage the focused localized features processed by the masked attention and enrich these features with further contextual or supplementary data.

Lastly after the attention mechanisms—both masked and cross-attention—the FFN acts as a point of non-linear transformation that further processes the refined, attention-focused features. This structure allows the FFN to introduce additional complexity and abstraction capabilities into the feature representations.

In order to maximize the capabilities of this model we had to create a custom loss function that takes into consideration all the data created by the model. The loss function for the Extended Mask2Former model is designed to jointly optimize object detection and instance segmentation tasks by integrating multiple loss components. The total loss  $L_{\text{total}}$  is computed as a weighted sum of the mask loss, bounding box regression loss, and classification loss:

$$L_{\text{total}} = \lambda_{\text{mask}} L_{\text{mask}} + \lambda_{\text{bbox}} L_{\text{bbox}} + \lambda_{\text{class}} L_{\text{class}} \quad (9)$$

where:

$\lambda_{\text{mask}}$ ,  $\lambda_{\text{bbox}}$ , and  $\lambda_{\text{class}}$  are weighting coefficients for each loss component.

## 1. Mask Loss:

The mask loss measures the discrepancy between the predicted masks  $\hat{M}$  and the ground truth masks  $M$ . It uses the Binary Cross-Entropy Loss with logits:

$$L_{\text{mask}} = \frac{1}{N} \sum_{i=1}^N \text{BCEWithLogits} \left( \hat{M}_i, M_i \right) \quad (10)$$

- $N$  is the number of matched instances.
- The matching between predicted and ground truth masks is performed using the Hungarian algorithm based on a combined cost of mask Intersection over Union (IoU) and classification cost.

## 2. Matching via Hungarian Algorithm:

To align predicted instances with ground truth instances, the Hungarian algorithm solves an assignment problem using a combined cost matrix  $\mathbf{C}$ :

$$\mathbf{C} = \alpha \left( 1 - \text{IoU} \left( \hat{M}, M \right) \right) + \beta \left( -\log \left( \text{Softmax} \left( \hat{C}_{\text{mask}} \right) + \epsilon \right) \right) \quad (11)$$

- $\alpha$  and  $\beta$  are weighting coefficients for the IoU and classification cost components, respectively.
- $\text{IoU} \left( \hat{M}, M \right)$  computes the Intersection over Union between predicted and ground truth masks.
- The negative log-likelihood term penalizes incorrect class predictions.
- $\epsilon$  is a small constant added to avoid taking the logarithm of zero.

## 3. Bounding Box Regression Loss:

This loss quantifies the error between the predicted bounding boxes  $\hat{B}$  and the regression targets  $B^*$  (encoded ground truth boxes relative to anchor boxes  $A$ ) using the Smooth L1 Loss:

$$L_{\text{bbox}} = \frac{1}{K} \sum_{j=1}^K \text{SmoothL1} \left( \hat{B}_j, B_j^* \right) \quad (12)$$

- $K$  is the number of anchor boxes.
- The regression targets  $B^*$  are obtained by encoding the matched ground truth boxes  $B$  with respect to the anchors  $A$ :

$$B^* = \text{encode} (B, A) \quad (13)$$

- Anchors are matched to ground truth boxes using an IoU-based matching strategy.

## 4. Classification Loss:

The classification loss evaluates the discrepancy between the combined class predictions  $\hat{C}$  and the ground truth class labels  $C$ . The predictions from both the bounding box branch  $\hat{C}_{\text{bbox}}$  and the mask branch  $\hat{C}_{\text{mask}}$  are combined by taking the element-wise maximum of their softmax probabilities:

$$\hat{C} = \max \left( \text{Softmax} \left( \hat{C}_{\text{bbox}} \right), \text{Softmax} \left( \hat{C}_{\text{mask}} \right) \right) \quad (14)$$

The classification loss is then computed using the Cross-Entropy Loss:

$$L_{\text{class}} = \frac{1}{N} \sum_{i=1}^N \text{CrossEntropy} \left( \hat{C}_i, C_i \right) \quad (15)$$

- $N$  is the number of instances.
- $C_i$  is the ground truth class label for instance  $i$ .

This multi-task learning approach leverages the shared representations between tasks, leading to better generalization and performance compared to training each task separately. It allows the model to learn more robust and comprehensive features from the data, as the different tasks provide complementary information that enriches the learning process. By leveraging both mask predictions and bounding box regressions, the model maximizes the use of all available data from small objects. Specifically, this combined approach addresses the challenges posed by small objects, which often provide limited information due to their size. The masks capture fine-grained spatial details that might be overlooked in bounding box predictions, enhancing the accuracy of segmentation for small objects. Meanwhile, the bounding boxes provide coarse localization that can guide the mask predictions, improving robustness in detecting small objects. This synergy allows the model to effectively detect and segment small objects, enhancing both accuracy and robustness in scenarios where small object recognition is critical.

The table below, sorted by the number of parameters, provides a comparative look at various popular object detection models that we have presented in the section above. This table highlights models ranging from YOLOv3, known for its balance of speed and accuracy, to more complex architectures like Mask R-CNN, which provides high precision at the cost of increased computational resources. Notably, the Extended Masked-Attention Mask Transformer shows how recent advancements aim to reduce parameter counts while potentially enhancing model capabilities. This spectrum illustrates the trade-offs between model complexity and operational efficiency, guiding decisions in model selection based on specific application needs.

Model	Number of Parameters (millions)
YOLO (You Only Look Once)	62
Extended Masked-Attention Mask Transformer	76.6
Single Shot Multibox Detector (SSD)	Typically around 100
Fast R-CNN	Typically around 150
Faster R-CNN	Typically around 200
FPN with Basic Detector	Typically around 200
Mask R-CNN	Typically around 250
R-CNN	Varies, typically less than 250

Table 3.1: Comparison of Object Detection Models Sorted by Number of Parameters

# 4 Experiments

In the experimental phase, we selected datasets that have previously been utilized in well-recognized competitions. This allows us to benchmark the performance of our model against established baselines and leading-edge results within the field, helping us make meaningful comparisons with our model. Each dataset employed in our experiments represents a common scenario in the field of object detection, encompassing diverse environments and perspective urban life captured through ground-level cameras, aerial views provided by drones, and wide-ranging perspectives from satellites.

## 4.1 Datasets

For the benchmarking of our model we decided to use three very well known datasets, and we are going to analyze in this section.

### 4.1.1 Microsoft Common Object in COntext (MS COCO)

The Microsoft Common Objects in Context (MS COCO) dataset 2017 [6] is a comprehensive image dataset designed for object detection, segmentation, and captioning tasks. It is known for its complexity of its images, which are primarily sourced from everyday scenes. The dataset includes 80 object categories, providing a wide range of common objects for robust training and evaluation of machine learning models. These categories encompass various items from person, bicycle, car, to stop sign and smaller objects like toothbrush.

In terms of its composition, the MS COCO 2017 dataset contains over 118,000 training images, 5,000 validation images, and a test set of around 41,000 images, bringing its total to approximately 164,000 images. This dataset is also accompanied by over 1.5 million object instances, each annotated. The annotations are formatted to support both object detection and instance segmentation tasks. Specifically, for object detection, each annotation includes not only the class label and a bounding box defined by the  $x$  and  $y$  coordinates of the top-left corner, width, and height, but also a detailed segmentation mask for each object instance, making it suitable for more granular segmentation tasks as well.

The dataset is divided into training, validation, and test splits to facilitate the training and fine-tuning of models in a structured manner. This split ensures that models can be trained on a large set of images and parameters can be fine-tuned on the validation set before final evaluations are performed on the test set. The use of MS COCO for competition and research has helped advance the field of computer vision by providing a challenging set of images and annotations that test the limits of both existing and novel visual recognition models.

Class Distribution in COCO 2017:

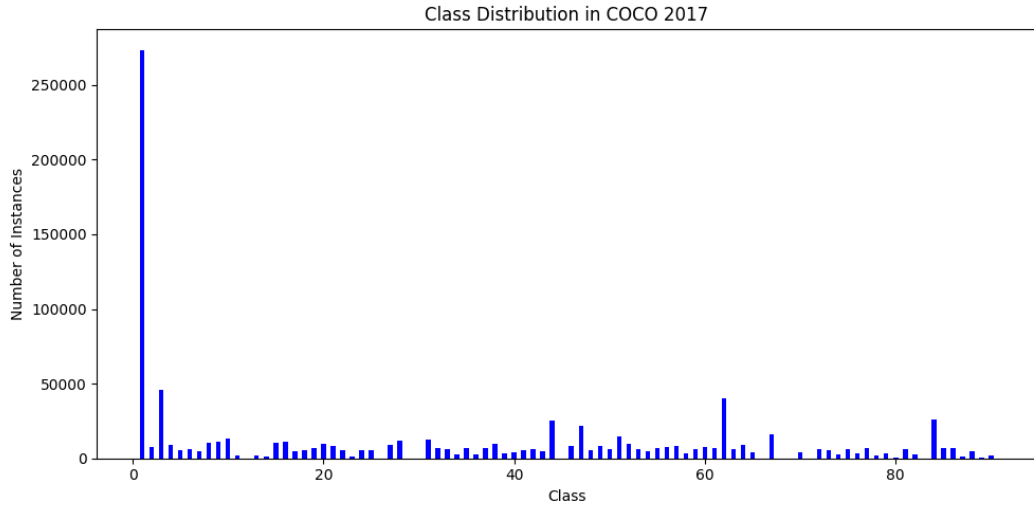


Figure 4.1: Class Distribution in COCO 2017

Calculating the mean and standard deviation of the bounding boxes and masks is crucial for generating more precise anchors, as it allows us to tailor the anchor sizes and aspect ratios to the actual distribution of objects in the dataset. This not only improves detection accuracy by aligning the anchors more closely with the objects, but also reduces unnecessary complexity by minimizing the need for an excessive number of anchors, which can lead to increased computational cost without performance gains. With that point in mind we calculated and store the following:

Metric	Number of Pixel
Mean Width	100
Mean Height	104
Width Standard Deviation	123
Height Standard Deviation	111

Table 4.1: Basic statistics of COCO dataset bounding boxes

### 4.1.2 Unmanned Aerial Vehicle Small Object Detection

The UAV-SOD (Unmanned Aerial Vehicle Small Object Detection) [20] dataset is specifically designed for advancing research in the area of object detection using aerial imagery captured by drones. This dataset focuses on the detection of small objects, which presents unique challenges due to the small scale and often complex backgrounds seen in aerial images. Here are the key details about the UAV-SOD dataset. The UAV-SOD dataset includes detailed annotations for each image, essential for supervised machine learning models such as object detectors. Annotations are provided in XML format compatible with the PASCAL VOC annotation format, which is widely used in object detection tasks. These annotations include bounding boxes that specify the coordinates of each object in the image. The objects in this dataset are annotated with their class labels, enabling not only object detection tasks but also potential use for object classification and segmentation challenges.

Class Distribution in UAV Small Object Detection:

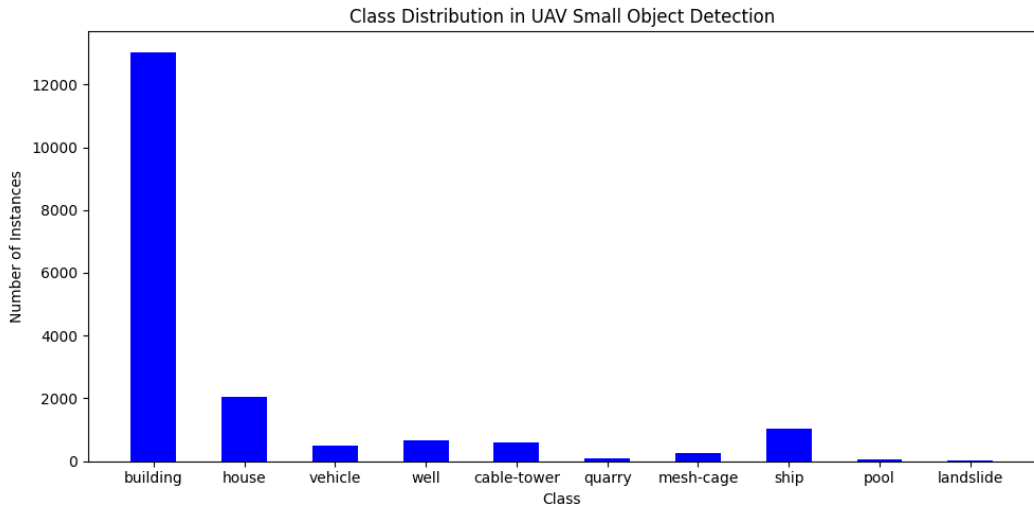


Figure 4.2: Class Distribution in UAV Small Object Detection

Once again computing the mean and standard deviation of the bounding boxes and masks helps ensure that the anchors are appropriately scaled to the objects in the dataset, reducing unnecessary complexity in the model.

Metric	Number of Pixel
Mean Width	19
Mean Height	19
Width Standard Deviation	16
Height Standard Deviation	17

Table 4.2: Basic statistics of UAV-SOD dataset bounding boxes

### 4.1.3 VisDrone

VisDrone [7] is a dataset designed for drone-based object detection, featuring 10,209 images captured across various environments using different types of drones. Each image in the dataset has a high resolution of  $2000 \times 1500$  pixels. The dataset is organized into splits for comprehensive training and evaluation, consisting of 6,471 images for training, 548 images for validation, and 3,190 images for testing. VisDrone includes a diverse set of ten object classes, such as pedestrians, cars, vans, buses, trucks, motorcycles, bicycles, awning-tricycles, and tricycles. This wide range of categories, combined with the diverse aerial perspectives provided by drone capture, makes VisDrone an ideal resource for developing and benchmarking deep learning models focused on enhancing object detection capabilities in drone surveillance systems.

Class Distribution in VIS Drone:

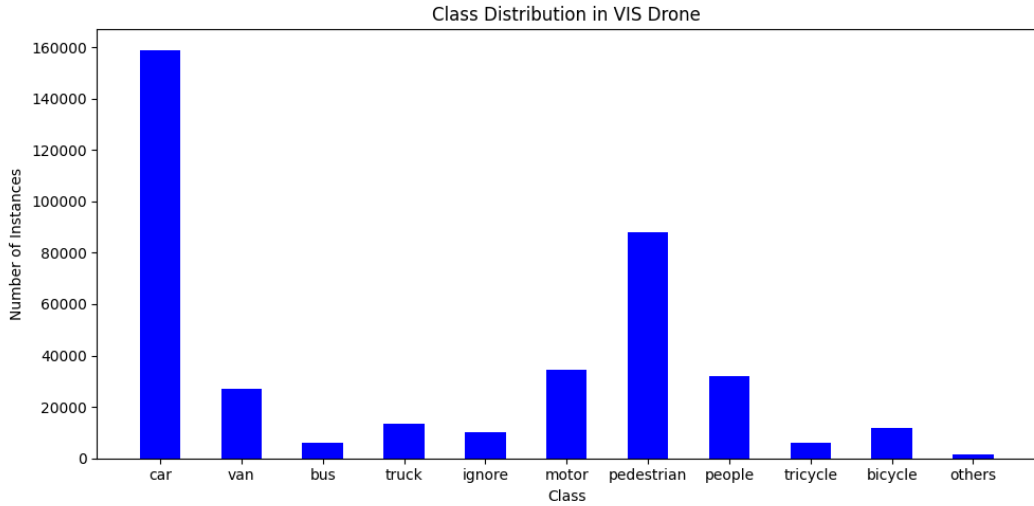


Figure 4.3: Class Distribution in VIS Drone

By determining the mean and standard deviation of the bounding boxes and masks, we optimize the anchor generation process, leading to more efficient object detection without adding unnecessary complexity. These variations convey the same core idea but in a more concise manner, assuming the main explanation has already been provided for the first dataset.

Metric	Number of Pixel
Mean Width	15
Mean Height	14
Width Standard Deviation	16
Height Standard Deviation	13

Table 4.3: Basic statistics of VisDrone dataset bounding boxes

From what we can detect in the class distributions, a significant class imbalance is present in the datasets. Class imbalance poses a challenge in training because models trained on such data may develop a bias towards more common classes and perform poorly on rare classes. We have to take this into consideration when choosing the evaluation metrics that give a more nuanced view of class-specific performance, such as per-class accuracy, are crucial for assessing a model’s true effectiveness across the varied classes present in these datasets. Finally the COCO 2017 dataset is commonly used as a benchmark in object detection tasks, though it is not specifically designed for small object detection. The mean and standard deviation of its bounding box sizes indicate that it includes a wider range of object sizes, with many larger objects. While the COCO dataset is useful for evaluating general object detection performance, datasets like UAV-SOD and VisDrone are more focused on small object detection, as reflected in their much smaller average bounding box sizes, making them more appropriate for detecting smaller objects in complex environments.

## 4.2 Data Pre-Processing

To ensure that the object detection models are trained on well-structured and uniform data, pre-processing steps are applied to standardize and enhance the raw dataset inputs. This process is crucial for achieving optimal model performance and is applied consistently across different datasets, such as COCO2017, UAV-SOD Drone, and Vis-Drone datasets, with specific adjustments tailored to each dataset's unique characteristics.

Firstly we have some general pre-processing steps applied across all datasets in order to make the training procedure

1. Resizing Images and Annotations: All images and corresponding annotations are resized to a uniform size of  $600 \times 600$  pixels. This standardization helps maintain consistency across the dataset, which is crucial for the feature map creation with the Efficient-B7 model. The resizing function also handles the segmentation data associated with each image, ensuring that all spatial information (bounding boxes and segmentation masks) is correctly scaled and translated according to the new image dimensions.
2. Image Padding: To maintain aspect ratio without distorting the image content, padding is applied using the most common color found in the image. This approach prevents the introduction of biases that could occur if a non-representative color was used.
3. Annotation Format: The annotation files for all the datasets have a common format in order to avoid any problems with the training process. The format is the following:  $x_{min}, y_{min}, x_{max}, y_{max}$ , class code,  $[(x_1, y_1), (x_2, y_2), \dots, (x_n, y_n)]$ , where the first four values are the bounding box coordinates following the Pascal VOC format, then we have class code of the object and lastly the list of coordinates describing the mask of the object.
4. Mask Creation: The masks are a vital part of the model, since we want to use the functionality of the Masked-Attention Mask Transformer in combination with the bounding box functionality to get better and more detailed results. The datasets ViS-Drone and Unmanned Aerial Vehicle datasets do not include masks and in order to have mask data we generate masks from the bounding box data. More specifically the mask data format is the following:  
 $[(x_{min}, y_{min}), (x_{min}, y_{max}), (x_{max}, y_{min}), (x_{max}, y_{max})]$
5. Calculation of Mean and Standard Deviation: For normalization purposes, the mean and standard deviation of the pixel values across the dataset are computed. These statistics are essential for normalizing the images during the model training process, allowing for faster convergence and improved generalization.
6. Visualization of Data: Functions are included to plot images alongside their annotations for both training and validation sets. This visual check allows for the verification of the correct processing and annotation of the data, ensuring integrity before training begins.

Furthermore we make specific changes to each dataset in order to ensure compatibility with the model. These changes are:

1. **COCO2017 Dataset** - Annotation Conversion: The original COCO annotations are converted into a simpler text format that includes bounding box coordinates and segmentation data. This conversion facilitates the use of custom training pipelines that may not natively support COCO’s complex annotation format.
2. **Vis-Drone Dataset** - Annotation Format Standardization: The annotations provided with the Vis-Drone dataset are standardized to ensure consistency with other datasets. This process includes recalculating bounding box coordinates from  $[x_{min}, y_{min}, width, height]$  to  $[(x_{min}, y_{min}), (x_{min}, y_{max}), (x_{max}, y_{min}), (x_{max}, y_{max})]$
3. **UAV-SOD Drone Dataset** - XML to Text Conversion: Given that UAV-SOD annotations might be provided in XML format, a conversion process is implemented to translate these XML files into a plain text format that is easier to manipulate and integrate into training workflows. The conversion also involves mapping categorical names to predefined numerical codes, which are crucial for consistent label encoding across different datasets.

These pre-processing steps are critical for preparing the data, ensuring that it meets the necessary format and quality standards required for effective model training. This comprehensive approach to data preparation helps in minimizing issues during training, leading to more robust and accurate object detection models.

### 4.3 Evaluation Metrics

Evaluation metrics are vital in object detection as they quantitatively measure a model’s accuracy, robustness, and effectiveness in predicting correct object locations and classifications. These metrics enable developers to compare different models, optimize parameters, and ensure that the system performs well across various conditions and datasets, guiding improvements and ensuring that the deployed models meet the required performance standards. Starting with the basic definitions we have:

1. True Positives (TP) [19] are the predictions that correctly match the class of the ground truth AND Confidence and IoU scores are higher than their thresholds.
2. False Positive (FP) [19] are the predictions that incorrectly predict a positive class when the ground truth is actually negative OR the IoU score is lower than the threshold.
3. False Negative (FN) [19] occurs when the model misses positive instances. It predicts a negative class when the ground truth is actually positive.
4. True Negative (TN) [19] represents instances where the confidence score of a detection that is not supposed to detect anything is lower than the threshold. This metric is not used in the object detection field since there are too many boxes that should not detect an object in an image.

The metrics we are going to be using that are object detection specific are the Average Precision (AP), mean Average Precision (mAP), Intersection over Union (IoU), Average Recall (AR) and mean Average Recall (mAR).

Recall [19] measures the proportion of actual positives that are correctly identified by the model, indicating the model's ability to detect all relevant instances.

$$\text{Recall} = \frac{TP}{TP + FN} \quad (16)$$

Precision [19] indicates the accuracy of the positive predictions made by the model, measuring the proportion of positive identifications that were actually correct.

$$\text{Precision} = \frac{TP}{TP + FP} \quad (17)$$

F1-Score [19] is the harmonic mean of precision and recall, providing a balance between the two by penalizing extreme values.

$$F1 = 2 \cdot \frac{\text{Precision} \times \text{Recall}}{\text{Precision} + \text{Recall}} \quad (18)$$

Intersection Over Union (IoU) [19] assesses the overlap between predicted bounding boxes and ground truth boxes, quantifying the exactness of the location of predictions. It is a fundamental metric for determining whether a detection is a true.

$$IoU = \frac{\text{Area of Overlap}}{\text{Area of Union}} \quad (19)$$

Average Precision (AP) [19] quantifies the precision of an object detector across different recall levels by taking the mean of precisions computed at the point of each of the 11 recall levels. The precision at each recall level  $r$  is interpolated by taking the maximum precision measured for a method at any recall level  $\geq r$

$$AP = \frac{1}{11} \sum_{r \in \{0.0, 0.1, \dots, 1.0\}} P_{\text{interp}}(r) \quad (20)$$

Mean Average Precision (mAP) [19] is the average of the AP scores for all classes or over different Intersection over Union (IoU) thresholds. This metric gives an overall effectiveness of the detection model across various object categories or detection precisions, making it ideal for scenarios where multiple object types are involved.

$$mAP = \frac{1}{N} \sum_{i=1}^N AP_i \quad (21)$$

## 4.4 Training

To implement the Extended Masked-Attention Mask Transformer, we utilized Amazon Web Services (AWS) SageMaker for efficient training and experimentation. Specifically, we employed the *ml.p4d.24xlarge* instance type for our notebook environment, which is equipped with eight NVIDIA A100 GPUs and supports CUDA 12.1. This powerful computational setup allowed us to run the training with a batch size of four images per batch, achieving an optimal balance between convergence speed and model accuracy.

The weights of the network were initialized using the default settings provided by PyTorch, ensuring standard initialization practices. All experiments were conducted using this configuration to maintain consistency and reliability in our results. By leveraging the capabilities of AWS SageMaker and the high-performance computing resources of the *ml.p4d.24xlarge* instance, we were able to efficiently train the model and effectively utilize the limited data from small objects in images.

To provide clarity on our training setup and ensure reproducibility, the table 4.4 summarizes the key training parameters used for the Extended Masked-Attention Mask Transformer. These parameters were carefully selected based on extensive experimentation to achieve an optimal balance between convergence speed and model accuracy.

	<b>MS COCO</b>	<b>UAV-SOD</b>	<b>VisDrone</b>
Number of Epochs	125	75	75
Optimizer	AdamW	AdamW	AdamW
Learning Rate	$1 \times 10^{-4}$	$1 \times 10^{-3}$	$1 \times 10^{-3}$
Batch size	4	4	4
Image size	$600 \times 600$	$600 \times 600$	$600 \times 600$
Number of Anchors	30000	722	722

Table 4.4: Details of training parameters per dataset

## 4.5 Results

Following the comprehensive description of our training setup and parameters, we now present the results of our experiments with the Extended Masked-Attention Mask Transformer. This section delves into the performance metrics achieved by the model, highlighting its effectiveness in both object detection and instance segmentation tasks. We evaluate the model’s ability to accurately detect and segment objects of various sizes within images, with a particular focus on its performance on small objects, which pose significant challenges due to their limited visual information. For brevity and clarity, we will use the following abbreviations throughout:

- Masked-Attention Mask Transformer will be referred to as MAMT.
- Extended Masked-Attention Mask Transformer will be referred to as EMAMT.

The Mask2Former model has a Sliding Window (Swin-L) [15] backbone, pre-trained on the ImageNet-22K dataset, is the best performing model from the proposed Mask2Former variations that we will compare our model against. It operates with 200 queries and was trained for 100 epochs utilizing a total of 216 million parameters. This model is computationally intensive, requiring 868 gigaflops (FLOPS) and running at a speed of 4 frames per second (FPS). The use of a pre-trained Swin-L backbone adds significant power to its feature extraction, but the high number of parameters and FLOPS highlight the overall complexity and computational weight of the model, which can impact efficiency in high-performance tasks.

### 4.5.1 Microsoft Common Object in COntext (MS COCO)

As expected, the proposed methodology is significantly lighter than original Masked-Attention Mask Transformer, where our model is 56% lighter in terms of number of trainable parameters. This complexity reduction comes at a performance drop of around 6.5%, which is sensible given the great difference in parameters and complexity. We can see the performance of each model on the table 4.5 along with the mAP across IoU thresholds ranging from 0.5 to 0.95.

Model	mAP(@0.5)	mAP(@0.5:0.95)	Queries	Parameters	GFLOPs
EMAMT	44.5	30.2	100	95M	492
MAMT	<b>50.2</b>	<b>38.8</b>	200	216M	868

Table 4.5: Results of training for COCO dataset

On the plot seen on the Figure 4.4, both models demonstrate a rapid increase in mAP during the first 20 epochs, reflecting quick initial learning. Afterward, the mAP increases more gradually, indicating that the models are nearing convergence. The MAMT model consistently outperforms EMAMT in both metrics, achieving a higher final mAP. The mAP@0.5 performance of MAMT plateaus at around 50%, while EMAMT stabilizes at 41.5%. Similarly, for mAP@0.5:0.95, MAMT reaches approximately 39%, while EMAMT stabilizes around 30%.

These results highlight the trade-off between model complexity and performance. While EMAMT is a lighter model with fewer parameters, it shows a lower overall performance compared to MAMT, which has a larger parameter count and FLOPs.

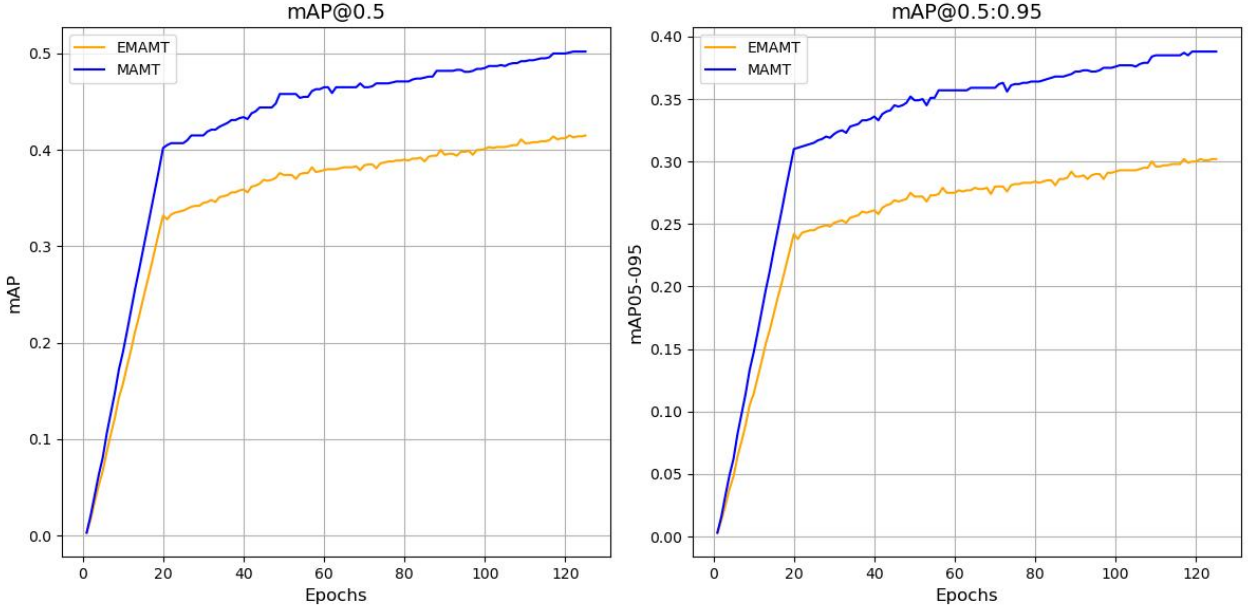


Figure 4.4: Performance comparison of MAMT and EMAMT on mAP at 50% IoU threshold (left) and the average mAP across IoU thresholds from 50% to 95% (right) for the COCO2017 dataset

#### 4.5.2 Unmanned Aerial Vehicle Small Object Detection

As seen with the COCO dataset, the proposed methodology is substantially lighter. In the UAV-SOD dataset, this reduction in complexity results in a slight performance improvement, with the EMAMT model outperforming MAMT by a margin of 3.1% in mAP(@0.5) and 3.1% in mAP(@0.5:0.95). This result is particularly notable given the significant reduction in both parameters and FLOPs. The detailed results of the two models can be seen in Table 4.6, showing that our lighter model maintains strong performance even in small object detection tasks.

Model	mAP(@0.5)	mAP(@0.5:0.95)	Queries	Parameters	GFLOPs
EMAMT	<b>51.3</b>	<b>39.2</b>	100	95M	492
MAMT	48.2	36.1	200	216M	868

Table 4.6: Results of training for UAV-SOD dataset

Once again both models exhibit a sharp rise in mAP during the first 20 epochs as presented , which signifies efficient early learning. After this initial phase, the EMAMT model maintains a higher mAP throughout the training period compared to MAMT, indicating better performance in this dataset. The EMAMT model peaks at an mAP@0.5 of approximately 51%, while MAMT reaches around 48%. Similarly, for mAP@0.5:0.95, EMAMT stabilizes at around 39%, outperforming MAMT, which plateaus at 36%.

These results suggest that EMAMT, despite having fewer parameters, manages to deliver superior performance on small object detection tasks, such as in UAV-SOD, compared to the larger MAMT model. This highlights the potential of more efficient models to perform well in specialized scenarios where smaller objects dominate the dataset.

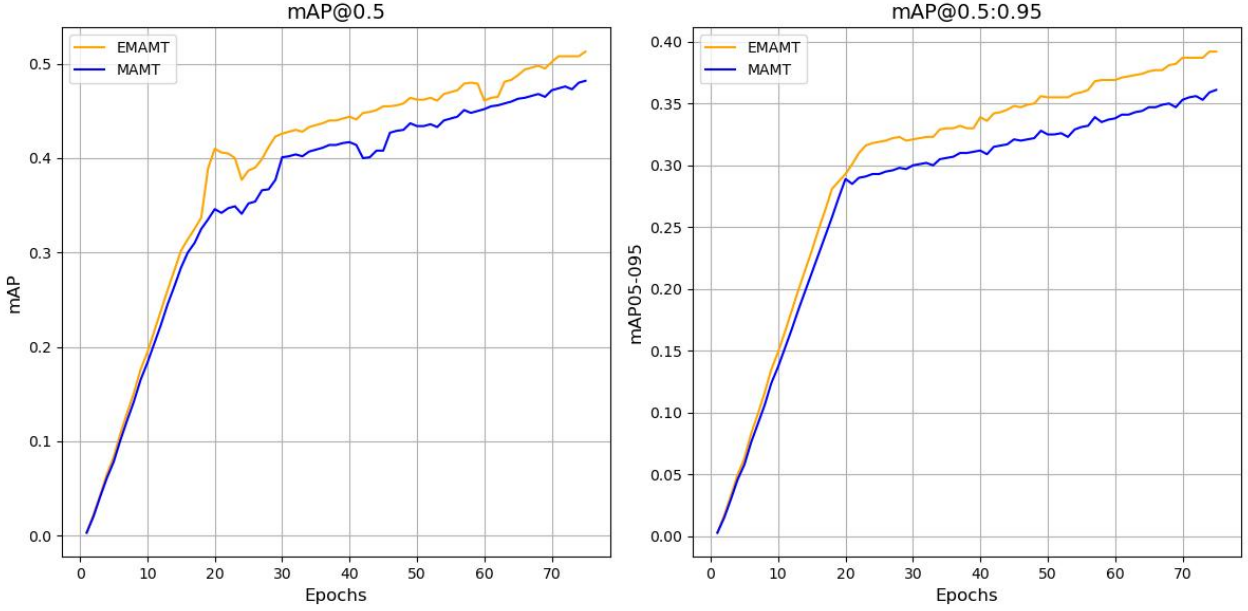


Figure 4.5: Performance comparison of MAMT and EMAMT on mAP at 50% IoU threshold (left) and the average mAP across IoU thresholds from 50% to 95% (right) for the UAV-SOD dataset

#### 4.5.3 VisDrone

Similar to the UAV-SOD dataset, the proposed EMAMT model achieves a significant reduction in trainable parameters, being 56% lighter than the original MAMT. However, in the VisDrone dataset, this comes at a noticeable performance trade-off, with a drop of around 13.7% in mAP(@0.5) and 10% in mAP(@0.5:0.95). Despite this reduction in performance, the lighter architecture of EMAMT offers benefits in terms of computational efficiency. As the table 4.7 summarizes the performance of both models, showcasing the balance between model complexity and detection performance on small object datasets.

Model	mAP(@0.5)	mAP(@0.5:0.95)	Queries	Parameters	GFLOPs
EMAMT	39.5	29.2	100	95M	492
MAMT	<b>53.2</b>	<b>39.2</b>	200	216M	868

Table 4.7: Results of training for VisDrone dataset

Similarly both models exhibit a sharp rise in performance during the first 20 epochs, with MAMT clearly outperforming EMAMT throughout the training. In the mAP@0.5 plot, MAMT reaches a higher final performance of approximately 53%, while EMAMT plateaus around 39%. Similarly, for mAP@0.5:0.95, MAMT achieves around 39%, while EMAMT settles at around 29%.

These results highlight the stronger performance of MAMT over EMAMT for object detection in the VisDrone dataset, which contains small and challenging objects. Despite being a lighter model, EMAMT shows a notable performance, but the more complex MAMT model offers a better ability to handle the intricacies of the dataset, as seen by the significant gap in both metrics.

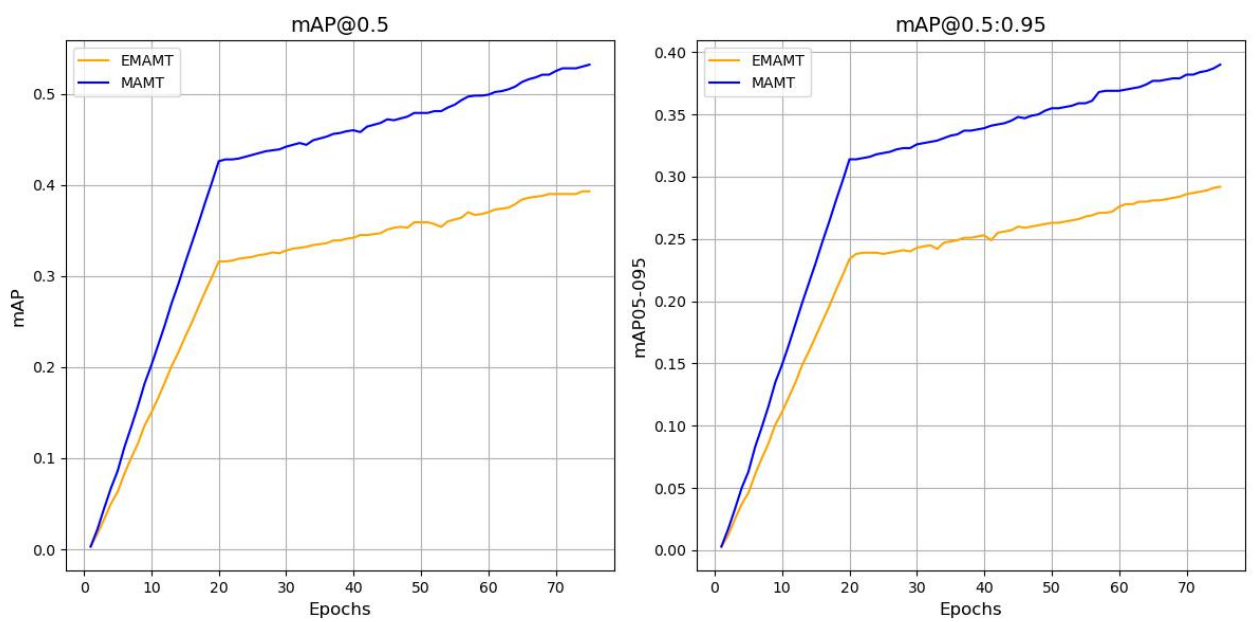


Figure 4.6: Performance comparison of MAMT and EMAMT on mAP at 50% IoU threshold (left) and the average mAP across IoU thresholds from 50% to 95% (right) for the VisDrone dataset

# 5 Discussion

## 5.0.1 Differences between models

The implementation and evaluation of the proposed method on the PANet and TPH-YOLOv5 models produced two different results on the model performances. It was extended that while the implementation of the proposed method on TPH-YOLOv5 significantly reduced the computational cost of the model with little loss in performance or even improvement in performance on a dataset with remote sensing images, the implementation of the method on PANet did not have as much improvement in computational cost and the loss in performance was higher.

This difference in results is observed due to the micro differences in the model architecture. PANet uses one prediction head for all 4 levels of the architecture while TPH-YOLO has a separate prediction head for each level. This negatively affects the model with the proposed method as due to the smaller paths the update of weights in the early layers of the model is more direct and the loss of one layer can affect the update of another layer more significantly. Another difference in the architecture of the two models is the size of the feature maps in the "neck" part of the models. PANet uses a fixed depth at all levels of the "neck" while TPH-YOLOv5 has different depths in the feature maps depending on the level in the feature pyramid. This enables TPH-YOLO to reduce the depth of the feature maps in the "neck" part using the proposed method while preserving the ability to preserve essential information. PANet on the other hand, due to the small depth of the feature maps (256-d) has a reduced ability to preserve essential information when applying the proposed method.

## 5.0.2 Performance difference between datasets

In the experiments conducted within the thesis, a difference in the results of the implementation of the proposed method in TPH-YOLOv5 between the VisDrone and AI-TOD datasets was observed. More precisely, the proposed method when tested on the VisDrone dataset showed a decrease in performance compared to the original TPH-YOLOv5 while in the tests performed on the AI-TOD dataset TPH-YOLOv5 with the proposed method showed an optimization in performance compared to the original. This is most likely due to the specificity of the VisDrone dataset. As shown in Figure 29, this dataset has many objects that have not been annotated. This leads the model to make "false" predictions, when in fact its predictions were correct. A model with a small gradient path is more affected by these "false" predictions as the error signal from the false predictions does not have to propagate through many layers before it reaches the early layers. This results in the model being more conservative in its predictions which can reduce recall. This phenomenon is not observed in models with longer gradient paths as the error signal has to propagate through more layers so the early layers are not affected by such "false" predictions.

# 6 Conclusion

In this thesis, we introduced a novel network-level gradient path design for object detection models, incorporating both ‘top-down’ and ‘bottom-up’ pathways in the network’s ‘neck’. This method is versatile, with applicability to both single-stage and multi-stage models. Upon evaluating the performance of the original models and their modified counterparts using our proposed method, we arrived at the following conclusions:

The application of our method to single-stage models results in a more significant reduction in computational resources compared to its application to multi-stage models.

- Despite its lower efficiency with multi-stage models, our proposed method can still be beneficial when the demand for computational resources outweighs the need for model precision.
- The modified two-stage model, while being 9.51version, does exhibit a decrease in performance. Specifically, its mAP at a 0.5 IoU threshold is at least 7.8thresholds from 0.5 to 0.95 is at least 3.6
- The one-stage model, when modified with our proposed method, becomes 32.671.60.5 to 0.95.
- Interestingly, on a remote sensing images dataset, the performance of the modified one-stage model improves by at least 6.3threshold and by 2.40.95. In future work, we intend to further investigate the performance differences that we have noticed between the single-stage and two-stage models. A key question that emerged from our study is why the two-stage model did not yield similar results to the single-stage model. Unravelling this mystery will be a primary focus,

as it has the potential to yield a useful understanding of the fundamental mechanics of these models and inspire future techniques for optimisation. Additionally, we plan to work on enhancing the performance of multi-stage models. While our proposed method showed promising results with single-stage models, its effectiveness was less noticeable when used with multi-stage models. We believe there is potential for improvement in this area. Lastly, to ensure the generalizability of our findings, we intend to experiment with a broader range of single-stage models, including various versions of YOLO. This will help us determine whether the results obtained from the TPH-YOLOv5 model apply to a diverse range of models, thereby solidifying the robustness of our proposed method.

# Bibliography

- [1] Yang Bai et al. “Weak Target Detection in High-Resolution Remote Sensing Images by Combining Super-Resolution and Deformable FPN”. In: *IGARSS 2020 - 2020 IEEE International Geoscience and Remote Sensing Symposium*. 2020, pp. 292–295. DOI: [10.1109/IGARSS39084.2020.9323260](https://doi.org/10.1109/IGARSS39084.2020.9323260).
- [2] B. Bosquet, M. Muentes, and V. M. Brea. “STDnet: exploiting high resolution feature maps for small object detection”. In: *Engineering Applications of Artificial Intelligence* 91 (2020), p. 103615.
- [3] Nicolas Carion et al. *End-to-End Object Detection with Transformers*. 2020. arXiv: [2005.12872 \[cs.CV\]](https://arxiv.org/abs/2005.12872). URL: <https://arxiv.org/abs/2005.12872>.
- [4] Bowen Cheng, Alexander G. Schwing, and Alexander Kirillov. *Per-Pixel Classification is Not All You Need for Semantic Segmentation*. 2021. arXiv: [2107.06278 \[cs.CV\]](https://arxiv.org/abs/2107.06278). URL: <https://arxiv.org/abs/2107.06278>.
- [5] Bowen Cheng et al. *Masked-attention Mask Transformer for Universal Image Segmentation*. 2022. arXiv: [2112.01527 \[cs.CV\]](https://arxiv.org/abs/2112.01527). URL: <https://arxiv.org/abs/2112.01527>.
- [6] COCO Consortium. *COCO Dataset*. <https://cocodataset.org/#download>. Accessed: 2024-09-22.
- [7] VisDrone Consortium. *VisDrone Dataset*. <https://github.com/VisDrone/VisDrone-Dataset>. Accessed: 2024-09-22.
- [8] Chunfang Deng et al. *Extended Feature Pyramid Network for Small Object Detection*. 2020. arXiv: [2003.07021 \[cs.CV\]](https://arxiv.org/abs/2003.07021). URL: <https://arxiv.org/abs/2003.07021>.
- [9] Alexey Dosovitskiy et al. *An Image is Worth 16x16 Words: Transformers for Image Recognition at Scale*. 2021. arXiv: [2010.11929 \[cs.CV\]](https://arxiv.org/abs/2010.11929). URL: <https://arxiv.org/abs/2010.11929>.
- [10] Yuxin Fang et al. *Instances as Queries*. 2021. arXiv: [2105.01928 \[cs.CV\]](https://arxiv.org/abs/2105.01928). URL: <https://arxiv.org/abs/2105.01928>.
- [11] Ross Girshick. *Fast R-CNN*. 2015. arXiv: [1504.08083 \[cs.CV\]](https://arxiv.org/abs/1504.08083). URL: <https://arxiv.org/abs/1504.08083>.
- [12] Ross Girshick et al. *Rich feature hierarchies for accurate object detection and semantic segmentation*. 2014. arXiv: [1311.2524 \[cs.CV\]](https://arxiv.org/abs/1311.2524). URL: <https://arxiv.org/abs/1311.2524>.
- [13] Kaiming He et al. *Mask R-CNN*. 2018. arXiv: [1703.06870 \[cs.CV\]](https://arxiv.org/abs/1703.06870). URL: <https://arxiv.org/abs/1703.06870>.
- [14] Shihua Huang et al. *FaPN: Feature-aligned Pyramid Network for Dense Image Prediction*. 2021. arXiv: [2108.07058 \[cs.CV\]](https://arxiv.org/abs/2108.07058). URL: <https://arxiv.org/abs/2108.07058>.

- [15] Gang Li et al. *SimViT: Exploring a Simple Vision Transformer with sliding windows*. 2021. arXiv: [2112.13085 \[cs.CV\]](https://arxiv.org/abs/2112.13085). URL: <https://arxiv.org/abs/2112.13085>.
- [16] Tsung-Yi Lin et al. *Feature Pyramid Networks for Object Detection*. 2017. arXiv: [1612.03144 \[cs.CV\]](https://arxiv.org/abs/1612.03144). URL: <https://arxiv.org/abs/1612.03144>.
- [17] Wei Liu et al. “SSD: Single Shot MultiBox Detector”. In: *Computer Vision – ECCV 2016*. Springer International Publishing, 2016, pp. 21–37. ISBN: 9783319464480. DOI: [10.1007/978-3-319-46448-0\\_2](https://doi.org/10.1007/978-3-319-46448-0_2). URL: [http://dx.doi.org/10.1007/978-3-319-46448-0\\_2](http://dx.doi.org/10.1007/978-3-319-46448-0_2).
- [18] Keiron O’Shea and Ryan Nash. *An Introduction to Convolutional Neural Networks*. 2015. arXiv: [1511.08458 \[cs.NE\]](https://arxiv.org/abs/1511.08458). URL: <https://arxiv.org/abs/1511.08458>.
- [19] Rafael Padilla, Sergio L. Netto, and Eduardo A. B. da Silva. “A Survey on Performance Metrics for Object-Detection Algorithms”. In: *2020 International Conference on Systems, Signals and Image Processing (IWSSIP)*. 2020, pp. 237–242. DOI: [10.1109/IWSSIP48289.2020.9145130](https://doi.org/10.1109/IWSSIP48289.2020.9145130).
- [20] Sovit Rath. *UAV Small Object Detection Dataset*. <https://www.kaggle.com/datasets/sovitrath/uav-small-object-detection-dataset>. Accessed: 2024-09-22.
- [21] Joseph Redmon et al. *You Only Look Once: Unified, Real-Time Object Detection*. 2016. arXiv: [1506.02640 \[cs.CV\]](https://arxiv.org/abs/1506.02640). URL: <https://arxiv.org/abs/1506.02640>.
- [22] S. Ren et al. “Faster R-CNN: Towards Real-Time Object Detection with Region Proposal Networks”. In: *Advances in Neural Information Processing Systems (NeurIPS)*. Montreal, Quebec, Canada, 2015.
- [23] Shaoqing Ren et al. *Faster R-CNN: Towards Real-Time Object Detection with Region Proposal Networks*. 2016. arXiv: [1506.01497 \[cs.CV\]](https://arxiv.org/abs/1506.01497). URL: <https://arxiv.org/abs/1506.01497>.
- [24] Robin Strudel et al. *Segmenter: Transformer for Semantic Segmentation*. 2021. arXiv: [2105.05633 \[cs.CV\]](https://arxiv.org/abs/2105.05633). URL: <https://arxiv.org/abs/2105.05633>.
- [25] Mingxing Tan and Quoc V. Le. *EfficientNet: Rethinking Model Scaling for Convolutional Neural Networks*. 2020. arXiv: [1905.11946 \[cs.LG\]](https://arxiv.org/abs/1905.11946). URL: <https://arxiv.org/abs/1905.11946>.

# A Appendix A